Chemical Science

ROYAL SOCIETY OF CHEMISTRY

PERSPECTIVE

View Article Online
View Journal | View Issue

Cite this: *Chem. Sci.*, 2020, **11**, 10553

All publication charges for this article have been paid for by the Royal Society of Chemistry

Received 25th March 2020
Accepted 15th July 2020

DOI: 10.1039/d0sc01721c

rsc.li/chemical-science

Grafted semiconducting polymer amphiphiles for multimodal optical imaging and combination phototherapy

Chen Xie,†[a] Wen Zhou,†[b] Ziling Zeng,[c] Quli Fan *[a] and Kanyi Pu *[c]

Semiconducting polymer nanoparticles (SPNs) have gained growing attention in biomedical applications. However, the preparation of SPNs is usually limited to nanoprecipitation in the presence of amphiphilic copolymers, which encounters the issue of dissociation. As an alternative to SPNs, grafted semiconducting polymer amphiphiles (SPAs) composed of a semiconducting polymer (SP) backbone and hydrophilic side chains show increased physiological stability and improved optical properties. This review summarizes recent advances in SPAs for cancer imaging and combination phototherapy. The applications of SPAs in optical imaging including fluorescence, photoacoustic, multimodal and activatable imaging are first described, followed by the discussion of applications in imaging-guided phototherapy and combination therapy, light-triggered drug delivery and gene regulation. At last, the conclusion and future prospects in this field are discussed.

1. Introduction

Cancer theranostics which integrates cancer imaging and therapy into one system provides the opportunity of continuous monitoring of therapeutic efficiency, thus allowing clinicians to design personalized medicine for each patient.[1,2] Among numerous imaging modalities, optical imaging which utilizes light as an excitation or signal source has gained more and more attention because of its advantages such as low toxicity, high sensitivity, low cost and minimal detection time.[3–7] Besides optical imaging, light can also trigger phototherapy including photodynamic therapy (PDT) and photothermal therapy (PTT), which are both promising therapeutic methods with the advantages of precise treatment and minimized side effects.[8–11] Thus, phototheranostics which combines optical imaging and phototherapy is a promising theranostic modality.[12–14] Until now, many materials have been developed as phototheranostic agents including near-infrared (NIR) dyes,[15–19] inorganic nanoparticles,[20,21] carbon and two-dimensional materials.[22–24] However, all of them have their own disadvantages such as poor photostability and low absorption coefficients.[25–27] Therefore, developing new optical agents with improved properties for phototheranostics is highly demanded.

Semiconducting polymers (SPs) are macromolecules with π-conjugated backbones, which have been widely applied in the fields of electronic devices and sensors because of their unique optical properties.[28] Recently, semiconducting polymer nanoparticles (SPNs) derived from SPs have been applied in optical imaging owing to their high absorption coefficient, good photostability and biocompatibility.[29–31] In detail, SPNs can be applied in fluorescence imaging including tumor imaging and cell tracking.[32–35] NIR-absorbing SPNs can be applied in photoacoustic (PA) imaging of stem cells,[36] vasculature,[37–39] tumor,[40–44] lymph nodes,[25,45] ROS[46,47] and pH.[48] Chemiluminescence and afterglow imaging of tumor,[49–53] reactive oxygen species (ROS),[54,55] temperature[56] and immunoactivation[57] can also be conducted by using SPNs with unique structures. In addition, SPNs with a high photothermal conversion efficiency (PCE) or singlet oxygen quantum yield can be used for PTT or PDT, respectively.[15,58–63] With such broad applications in optical imaging and phototherapy, numerous SPN-based nanoagents have been developed for phototheranostics, and most of them showed satisfactory efficacy.[64–70]

Despite the promise of SPNs in the field of cancer theranostics, some limitations still need to be overcome. The preparation of water-soluble SPNs is limited by encapsulating hydrophobic SPs into amphiphilic copolymers through nanoprecipitation.[71–73] Thus, such SPNs are in principle binary micelles. According to previous studies, micelles may dissociate in the blood circulation as the concentration of micelles may decrease significantly below the critical micelle concentration (CMC) in such an environment.[74] In addition, interactions with

[a]*Key Laboratory for Organic Electronics and Information Displays, Institute of Advanced Materials (IAM), Jiangsu National Synergetic Innovation Center for Advanced Materials (SICAM), Nanjing University of Posts & Telecommunications, Nanjing 210023, China. E-mail: iamqlfan@njupt.edu.cn*

[b]*State Key Laboratory of Medicinal Chemical Biology, College of Chemistry, Research Center for Analytical Sciences, Tianjin Key Laboratory of Molecular Recognition and Biosensing, Nankai University, Tianjin 300071, China*

[c]*School of Chemical and Biomedical Engineering, Nanyang Technological University, Singapore 637457. E-mail: kypu@ntu.edu.sg*

† These authors contributed equally to this work.

protein and other biological substances in the circulation may accelerate the micelle dissociation, leading to aggregation of hydrophobic SPs and poor biodistribution of nanoparticles.[75,76] Therefore, approaches to preparing structurally stable SPNs are highly desired.

To overcome the disadvantages of SPNs, grafted semiconducting polymer amphiphiles (SPAs) are designed and synthesized. SPAs are synthesized by grafting hydrophilic moieties onto the side chains of SPs. Such a structure enables SPAs to self-assemble in aqueous solution without the help of an amphiphilic copolymer, leading to a non-dissociable structure, improved optical properties and biodistribution profile compared with SPNs. Until now, the optical properties, preparation methods and biological applications of SPNs have been widely studied and reported in a number of reviews.[77,78] However, the synthesis, properties and applications of SPAs are rarely summarized. In this review, we summarize recent advances in the development of SPAs for cancer imaging and therapy. In the first part, we discuss the application and development of SPAs in molecular optical imaging, with fluorescence, PA, multimodal and activatable imaging being sequentially introduced. The second part discusses the applications of SPAs in phototheranostics including imaging-guided phototherapy and combination therapy, followed by light-triggered drug delivery and gene regulation. At last, a brief summary is given together with the discussion of the current status and potential challenges of this field.

2. Chemistry of SPAs

To synthesize SPAs, SPs with functional groups on the side chains should firstly be synthesized. Such kinds of SPs can be synthesized by using monomers with functional side chains. Copper-catalyzed click chemistry is the most commonly used method to graft hydrophilic moieties onto SPs, on account of its simple and highly efficient features.[79] Bromide-grafted SPs are first synthesized, followed by reacting with sodium azide to substitute bromide into azide. Azide-grafted SPs are then reacted with alkyne-modified hydrophilic moieties *via* a click reaction to give SPAs. Most SPAs were synthesized *via* such a procedure, such as SPA1-10, SPA14-17, SPA20, SPA22-24, and SPA27-33. The amidation reaction with a satisfactory reaction yield under mild reaction condition is another convenient reaction used to synthesize SPAs. For such a procedure, SPs with *tert*-butyl ester as the side chain are first synthesized, followed by deprotecting *tert*-butanol with trifluoroacetic acid (TFA) to give carboxyl-grafted SPs. The amidation reaction was then carried out between such SPs and amino-functionalized hydrophilic moieties to give SPAs (Fig. 1). SPA11-13 and SPA34 were synthesized *via* such a procedure. Most SPAs can directly dissolve into water and self-assemble into nanoparticles. In addition, SPAs can encapsulate hydrophobic drugs or photosensitizers to form theranostic nanosystems *via* nanoprecipitation.

3. Molecular optical imaging

Different hydrophilic moieties can be modified onto the side chains of SPs, such as polyglycerol (SPA1), poly(ethylene glycol) (PEG) (SPA2-11, SPA13-17), and chelator 6-hydrazinonicotinyl (SPA12) (Schemes 1 and 2). Most SPAs can be directly used as imaging contrast agents. To endow SPAs with the capability of afterglow imaging, photosensitizers were needed to be encapsulated into SPAs. For multimodal imaging, Gd^{3+} ions or radioactive elements should be chelated by SPAs. The hydrodynamic size of these SPAs ranged from several nanometers to hundreds of nanometers. For semiconducting oligomer-based SPAs, the size can reach as small as ~8 nm (SPA10). SPAs with relatively high PEG density may have a size of 20–40 nm. Also,

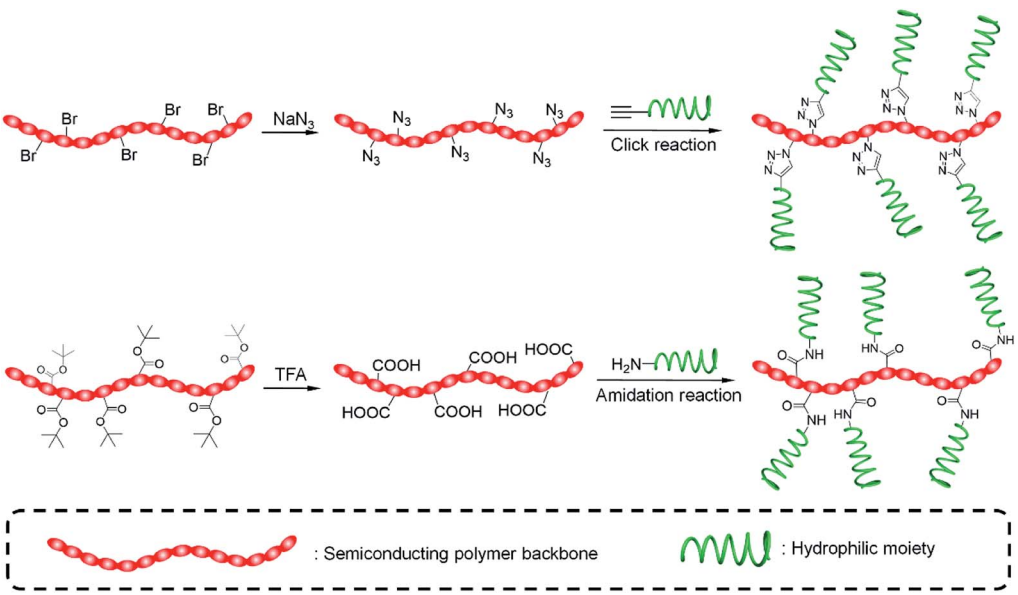

Fig. 1 Schematic illustration of SPAs prepared *via* click and amidation reactions.

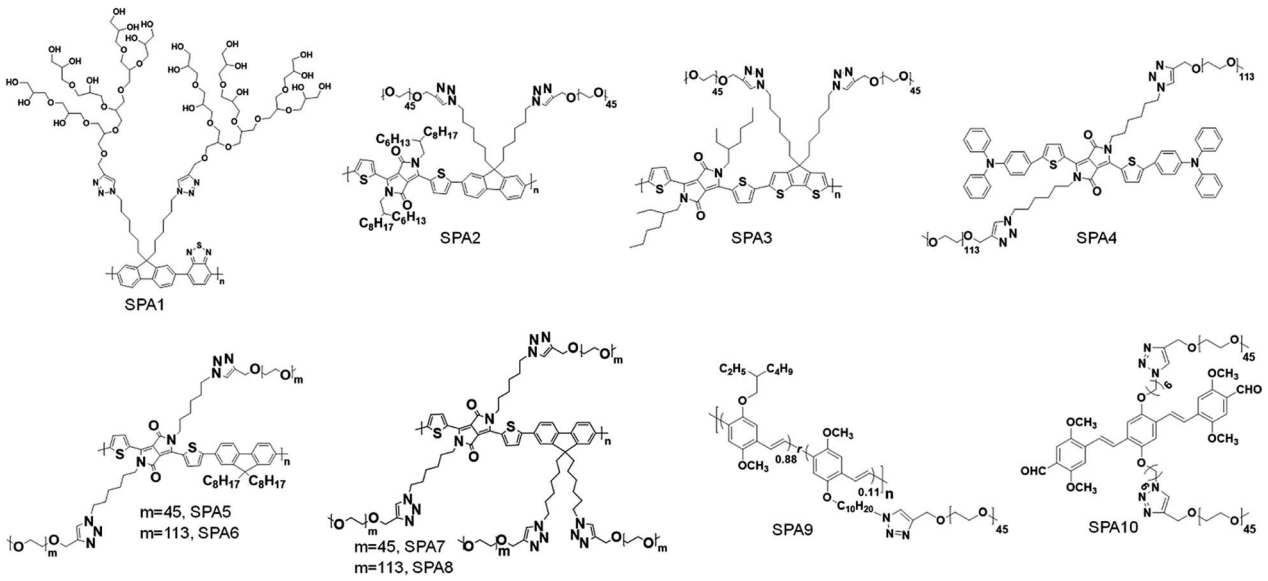

Scheme 1 Chemical structures of SPA1-10 for molecular optical imaging.

some SPAs had a size larger than 100 nm (SPA11), probably because of their low PEG density.

3.1. Fluorescence and PA imaging

Fluorescence imaging is a convenient and cost-effective optical imaging modality for disease diagnosis, fundamental biological research and real-time monitoring of therapeutic effects because of its high sensitivity and high temporal resolution.[80,81] Different from fluorescence imaging, PA imaging utilizes ultrasonic waves as the signal source and has a higher spatial resolution and deeper tissue penetration relative to fluorescence imaging.[82–84] Considering the complementary advantages of fluorescence and PA imaging, dual-modal imaging combining fluorescence and PA imaging has also gained more and more attention.[85,86]

Liu *et al.* synthesized fluorescent SPA1 with hyperbranched polyglycerol as the side chain. Owing to the strong fluorescence signal and good water solubility, SPA1 was applied for fluorescence cell imaging.[87] To synthesize SPAs for PA imaging, two SPAs (SPA2 and SPA3) containing diketopyrrolopyrrole (DPP) in the semiconducting backbone were designed. SPA3 with a higher PA intensity can be applied for *in vivo* PA imaging of tumor.[88] Compared with SPNs, semiconducting oligomer nanoparticles (SON) usually had a smaller hydrodynamic size, as the molecular weight of the semiconducting oligomer was lower than that of SPs. Therefore, a semiconducting oligomer-

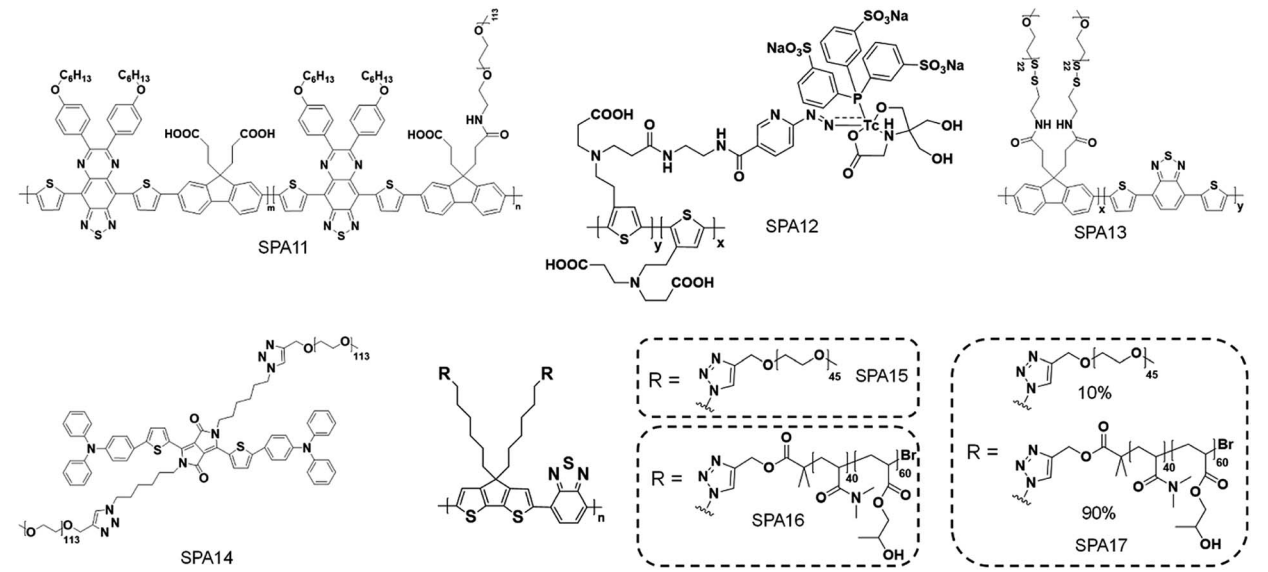

Scheme 2 Chemical structures of SPA11-17 for molecular optical imaging.

based SPA (SPA4) was designed and synthesized and can be used for *in vivo* fluorescence/PA dual-modal imaging.[89]

Grafting PEG onto SPs may change the conformation of SPs, thus affecting their optical properties. To study the influence of grafting density on the fluorescence and PA properties of SPAs, several SPAs (SPA5-8) with different PEG grafting densities were synthesized.[90] Poly(diketopyrrolopyrrole-*alt*-fluorene) (PDPPF) was used as the backbone of SPAs. All SPAs showed two vibronic peaks at 601 and 640 nm, which were slightly blue-shifted compared with that of PDPPF encapsulated by PEG-*b*-PPG-*b*-PEG (SPN1) (Fig. 2a). SPA7 had the highest fluorescence quantum yield (4.31%) among all the nanoparticles, followed by SPA8 (3.13%), SPA5 (2.77%), SPA6 (2.73%), and SPN1 (1.02%) (Fig. 2b). The fluorescence intensity of SPA7 was 11-fold higher than that of SPN1. In contrast, the PA amplitudes of all five nanoparticles at 680 nm were almost the same, which was approximately 4-fold higher than that of gold nanorods (GNRs) under the same concentrations of optical components (Fig. 2c). To understand the effect of PEG grafting density on the optical properties of SPAs, theoretical simulation was conducted to study the structures of SPAs. The results indicated that SPAs with a higher PEG density had a looser SP core when self-assembled in water, which can be attributed to the higher steric hindrance of the side chain for SPA7 than that for SPA5 (Fig. 2d). Therefore, the higher fluorescence intensity of SPA7 and SPA8 can be explained by their less aggregated SP cores, leading to less fluorescence quench compared with other SPAs.

With the highest fluorescence intensity and satisfactory PA amplitude, SPA7 was further applied for fluorescence and PA dual-modal imaging of tumor. After tail vein injection of SPA7, the fluorescence and PA signal in the tumor area of living mice gradually increased and reached a maximum at $t = 8$ h and 6 h, respectively (Fig. 2e and f). In addition, *ex vivo* biodistribution data for SPA7 indicated that tumor had the highest accumulation among all the major organs including the liver and spleen, indicating the excellent tumor accumulation capability of SPA7. The SPNs prepared by nanoprecipitation often had the highest accumulation in the liver. Therefore, such improved biodistribution of SPA7 may be attributed to its small hydrodynamic size (25 nm) and high PEG density.

3.2. Afterglow imaging

Although traditional optical imaging modalities such as fluorescence and PA imaging have shown great promise in the field of cancer diagnosis, some limitations still need to be overcome to further improve the diagnostic accuracy. One of the limitations is the low signal to background ratio (SBR) for both fluorescence and PA imaging, as they need real-time excitation during the imaging process.[91] Afterglow imaging is a novel imaging modality that detects luminescence emission after the removal of the excitation source. Thus, afterglow imaging can provide ultrahigh imaging sensitivity and deep tissue penetration with a minimum tissue background.[37,92]

To prepare SPA-based afterglow agents, we used polyphenylenevinylene (PPV) and PEG as the backbone and side chain, respectively, to give SPA9.[93] A NIR-absorbing photosensitizer (NCBS) was co-precipitated with SPA9 to form SPAN9 (Fig. 3a). Compared with PPVP prepared by nanoprecipitation of

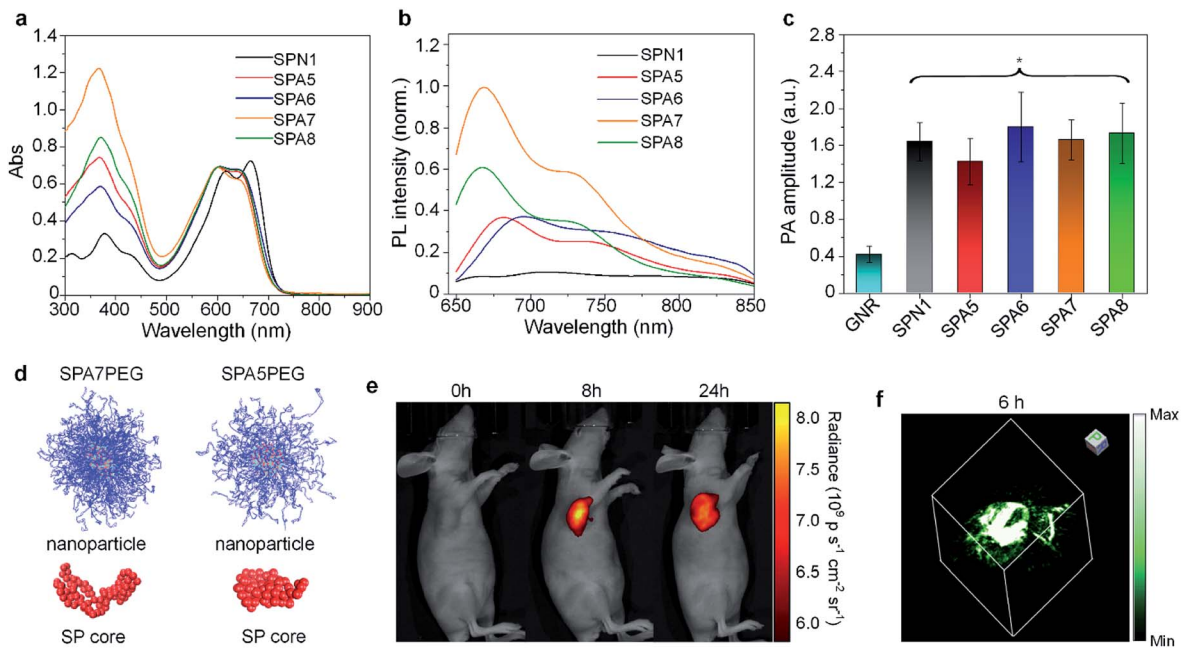

Fig. 2 Normalized absorption (a) and fluorescence (b) spectra of SP nanoparticles. (c) PA amplitudes of gold nanorods and SP nanoparticles under the same concentrations of optical components. (d) Simulated structures of nanoparticles and cores for SPA7PEG and SPA5PEG. (e) Representative fluorescence images of tumor bearing nude mice after i.v. injection of SPA7 at 0, 8, and 24 h. (f) Representative PA 3D image of tumor from SPA7-injected tumor bearing mice at $t = 6$ h post-injection. The error bars represent standard deviations of three different measurements. *No statistically significant difference. Adapted from ref. 90. Copyright© 2017 Wiley-VCH Verlag GmbH & Co. KGaA, Weinheim.

MEHPPV and NCBS in the presence of PEG-*b*-PPG-*b*-PEG, SPAN9 had a smaller hydrodynamic size (24 *vs.* 34 nm). SPAN9 and PPVP had similar absorption spectra, both showing two peaks at around 500 and 775 nm corresponding to the absorption of PPV and NCBS, respectively (Fig. 3b). The afterglow spectra of SPAN9 and PPVP were similar to their fluorescence spectra, and the afterglow intensity of SPAN9 was 1.3-fold higher than that of PPVP (Fig. 3c). The mechanism of afterglow signal generation for SPAN9 was similar to that in our previous study for PPVP. The generated singlet oxygen first reacts with double bonds of PPV with the resulting unstable intermediates being decomposed to release energy in the form of light.[37]

With strong NIR afterglow intensity, SPAN9 was then used for *in vivo* tumor imaging. To test the early diagnosis ability of SPAN9, the tumor volume was controlled to be ~5 mm^3. After i.v. injection of SPAN9 for 40 min, the afterglow images of mice can clearly show the position of tumor, while fluorescence images only showed the background signal. For PPVP-injected mice, afterglow images only showed the liver at such a time point, and the tumor can only be detected at 4 h post-injection (Fig. 3d). For both SPAN9 and PPVP-injected mice, the highest tumor accumulation of nanoparticles was detected at 24 h post-injection while the afterglow images of SPAN9-injected mice had a SBR of 306, 11-fold higher than that of fluorescence images (Fig. 3e). *Ex vivo* biodistribution study indicated that SPAN9 had higher accumulation in tumor than PPVP.

SPAN9 was then applied for metastatic tumor imaging owing to its superior ability of tumor detection. Peritoneal metastatic tumor-bearing mice were treated with SPAN9 or PPVP *via* i.v. injection, and fluorescence and afterglow images were captured at designated time points. The afterglow signal in the lower quadrant region gradually increased for SPAN9-injected mice, while no such increase was observed for PPVP-injected mice (Fig. 3f). At 1.5 h post-injection, skin and peritoneum of all mice were resected and the lower quadrant regions were imaged. Only autofluorescence can be detected for both SPAN9- and PPVP-injected mice. In contrast, strong afterglow spots can be detected on the intestine of SPAN9-injected mice, but no such signal was observed for PPVP-injected mice (Fig. 3g). H&E staining demonstrated that the tiny afterglow spots from SPAN9-injected mice were tumor tissues, which were hardly distinguished by the naked eye. Such results confirmed the fast detection of tiny metastatic tumors for SPAN9.

Based on the structure of oligophenylenevinylene (OPV), SPA10 was synthesized for *in vivo* afterglow imaging of biothiols.[94] SPA10 can react with cysteine or homocysteine by virtue of its aldehyde groups. Upon addition of cysteine, the fluorescence intensity of SPA10 increased by 25.2-fold, while its

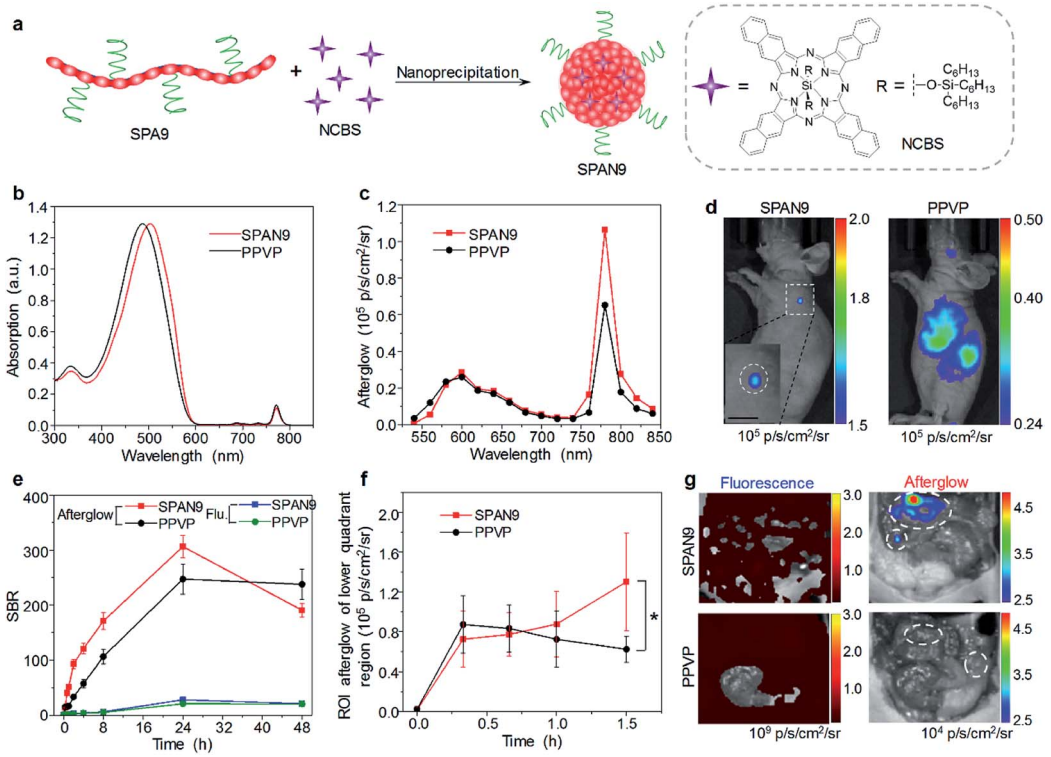

Fig. 3 (a) Schematic illustration for the preparation of SPAN9. (b) Absorption spectra of SPAN9 and PPVP in 1× PBS buffer (pH 7.4). (c) Afterglow spectra of SPAN9 and PPVP under the same mass concentration (130 μg mL^{-1}). (d) Afterglow images of living mice after i.v. injection of SPAN9 or PPVP for 40 min. (e) SBRs for fluorescence and afterglow imaging of tumor in living mice injected with SPAN9 or PPVP as a function of post-injection time. (f) Afterglow intensities of the lower quadrant region of living mice after i.v. injection of SPAN9 or PPVP as a function of post-injection time. (g) Fluorescence and afterglow images of abdominal cavity of mice after skin resection at 1.5 h post-injection of SPAN9 or PPVP. White circles mark the position of tumors. *Statistically significant difference ($p < 0.05$, $n = 3$). Error bars represent standard deviations of three different measurements ($n = 3$). Adapted from ref. 93. Copyright© 2018 Wiley-VCH Verlag GmbH & Co. KGaA, Weinheim.

afterglow intensity remained the same. With such a feature, SPA10 was applied for fluorescence imaging of cysteine in living cells. After encapsulation of NCBS, the absorption and emission of formed SPAN10 can be extended to the NIR region *via* fluorescence resonance energy transfer (FRET), which showed enhanced *in vivo* afterglow imaging of cysteine.

3.3. Multimodal imaging

Although optical imaging has shown great potential in biomedical applications, traditional imaging modalities such as magnetic resonance imaging (MRI) and X-ray computed tomography (CT) imaging have their own advantages and are irreplaceable in clinical diagnosis.[95] Thus, multimodal imaging which combines optical and traditional imaging modalities may provide better diagnostic efficacy than any single modality.

To combine MRI with optical imaging, SPA11 with PEG and carboxyl groups on the side chains was designed and synthesized.[96] Such a design endowed SPA11 with the ability of chelating Gd^{3+} ions to form SPAN11 with good water solubility (Fig. 4a). SPAN11 had an absorption peak at 760 nm and a NIR-II fluorescence emission peak at 1056 nm (Fig. 4b). The fluorescence quantum yield of SPAN11 was determined to be 0.38%. *In vitro* stability studies indicated that SPAN11 had superior photostability to indocyanine green (ICG). In addition, approximately 95% of Gd^{3+} ions remained within SPAN11 after 1 day incubation in PBS (pH 7.4), indicating the good physiological stability of SPAN11. The capability of multimodal imaging for SPAN11 was then studied. A linear correlation between PA intensity at 760 nm and the concentration of SPAN11 was observed, showing the feasibility for the quantification of PA signals. A similar trend for the MR signal was observed, and the magnetic relaxivity (r_1) of SPAN11 was calculated to be 10.95 mM^{-1} s^{-1}, which was significantly higher than that of the widely used Gd-DTPA contrast agent (4.40 mM^{-1} s^{-1}). Along with its satisfactory NIR-II fluorescence quantum yield mentioned above, SPAN11 was a good candidate for NIR-II fluorescence/PA/MRI tri-modal imaging.

SPAN11 was then applied for *in vivo* multimodal imaging, and 4T1 xenografted nude mice were used as the mouse model. Before injection of SPAN11, the tumor area of mice showed a weak background signal for both PA and T_1-weighted MRI imaging. After i.v. injection of SPAN11, both PA and MRI signals in the tumor area gradually increased over time, indicating the accumulation of SPAN11 into the tumor site (Fig. 4c). Compared

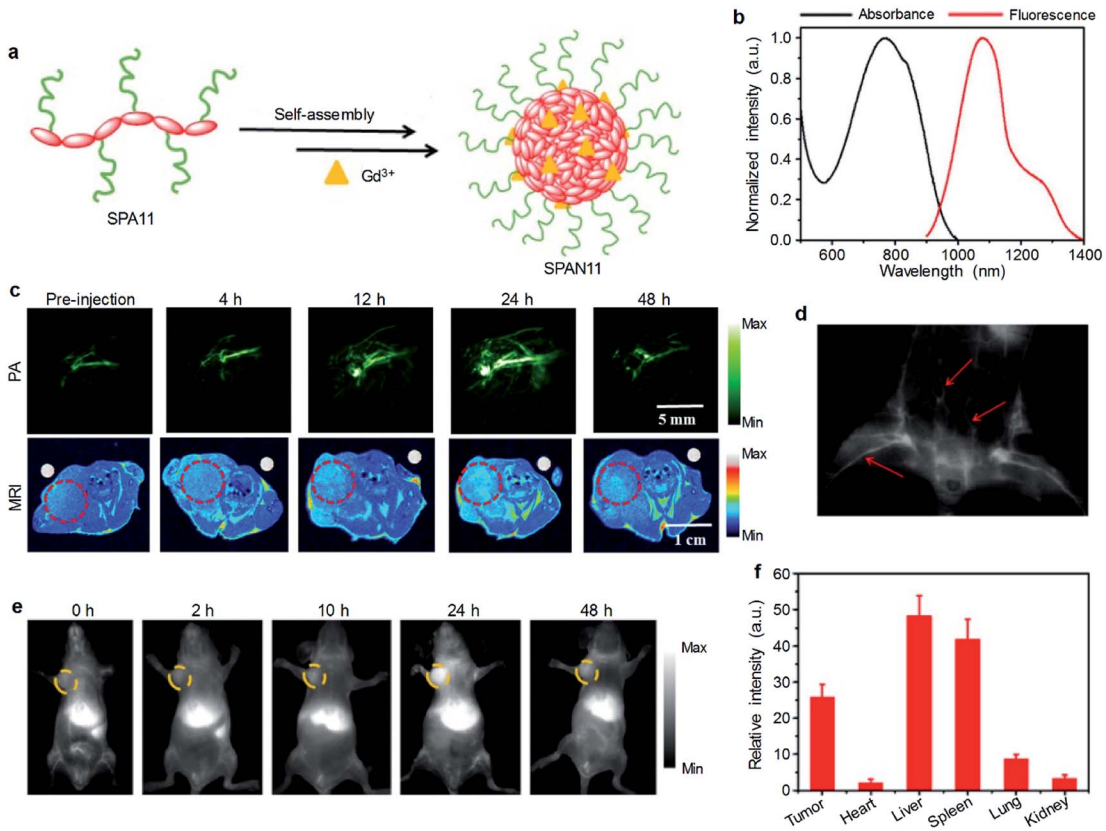

Fig. 4 (a) Schematic illustration for the preparation of SPAN11. (b) Absorption and emission spectra of SPAN11. (c) *In vivo* MRI and PA imaging of tumor bearing mice after i.v. injection of SPAN11 at different time points. The red circles indicate the position of tumor. (d) NIR-II fluorescence image of vascular tissues of a living mouse after i.v. injection of SPAN11 for 2 min under 808 nm laser excitation. The red arrows indicate blood vessels. (e) Representative NIR-II fluorescence images of 4T1 tumor bearing mice after i.v. injection of SPAN11 at different time points. The yellow circles indicate the position of tumor. (f) *Ex vivo* NIR-II fluorescence quantification of major organs from mice after 24 h post-injection of SPAN11. Error bars represent the standard deviations of three different measurements ($n = 3$). Adapted from ref. 96. Copyright© 2019 Ivyspring International Publisher.

with the commercially available T_1-weighted contrast agent Gd-DTPA, SPAN11 had a longer circulation time and higher tumor accumulation. These data demonstrated the efficient passive tumor accumulation and imaging capability of SPAN11.

Compared with NIR-I fluorescence imaging that utilizes wavelengths ranging from 700 to 900 nm, NIR-II fluorescence imaging which collects light beyond 1000 nm exhibits a higher spatial resolution and deeper tissue penetration.[97] SPAN11 was then applied for NIR-II fluorescence imaging by virtue of its long emission wavelength (1056 nm). After i.v. injection of SPAN11 for 2 min, the blood vessels of the whole body of mice can be lit up (Fig. 4d), indicating the circulation of SPAN11. Similar to the results of PA and MRI imaging, the NIR-II fluorescence signal in the tumor area gradually increased with the accumulation of SPAN11 (Fig. 4e). *Ex vivo* biodistribution of SPAN11 evaluated by NIR-II fluorescence imaging indicated that SPAN11 mainly accumulated in the liver, spleen and tumor (Fig. 4f). No damage to the major organs collected from SPAN11-injected mice was observed from H&E staining, indicating the good biocompatibility of SPAN11. In conclusion, SPAN11 can passively accumulate into the tumor site and be used as a multimodal imaging contrast agent for NIR-II fluorescence/PA/MRI imaging.

To achieve single-photon emission computed tomography (SPECT) and fluorescence dual-modal imaging, Wang *et al.* designed and synthesized SPA12.[98] SPA12 was composed of fluorescent polythiophene as the backbone and chelated radioactive ^{99m}Tc as the side chains. SPA12 can be applied for *in vivo* lymph node imaging. Strong SPECT signals can be detected in both draining axillary and lateral thoracic lymph nodes after paw injection. In addition, the fluorescence signal of SPA12 can also detect these two lymph nodes, and the background signal of SPA12 was much weaker than that of ICG, indicating its high accuracy for lymph node imaging.

3.4. Activatable imaging probes

Compared with "always-on" imaging probes, activatable imaging probes which emit signals in response to specific biomolecular targets or events of interest show many advantages such as a low background signal and concentration-independent contrast.[9] Cancer has been studied to be associated with the overexpression of many biomarkers such as glutathione (GSH), ROS and reactive nitrogen species (RNS).[99] Therefore, the development of activatable imaging probes for these substances has great significance in cancer diagnosis.

SPA13 was designed and synthesized for *in vitro* biothiol detection.[100] PEG was covalently linked onto the side chains of SPA13 *via* thiol-responsive disulfide bonds. Upon the addition of biothiols, the cleavage of disulfide bonds led to the release of PEG chains, causing aggregation of the backbone. Such aggregation improved the intramolecular FRET efficiency of SPA13, leading to increased and decreased fluorescence intensities at 628 and 420 nm, respectively. Such a feature endowed SPA13 with the ability of ratiometric fluorescence imaging of biothiols. To prepare nanoprobes for hypochlorite detection, semiconducting oligomer-based SPA14 was designed and synthesized.[101] SPA14 can encapsulate NCBS to form SPAN14. Upon treatment of hypochlorite, the phenothiazine-containing backbone of SPA14 was oxidized while NCBS remained intact, which led to the dramatic decrease of PA intensity at 680 nm but unchanged PA intensity at 780 nm. Such a feature endowed SPAN14 with the ability of ratiometric PA imaging of hypochlorite.

Besides internal stimuli such as biothiols and ROS, external stimuli, which are irrelevant to the microenvironment of probes, can also be utilized to turn on the signal of probes. For example, a thermo-responsive PA imaging probe, SPA17 with a NIR-absorbing SP, poly(cyclopentadithiophene-*alt*-benzothiadiazole) (PCPDTBT) as the backbone, was designed and synthesized.[102] The side chains of SPA17 were composed of 90% thermo-responsive PDMA-*r*-HPA and 10% PEG. Upon increasing the temperature, the hydrophilic PDMA-*r*-HPA became hydrophobic, leading to the aggregation of SPA17 and thus the enhancement of the PA signal (Fig. 5a). SPA15 and SPA16 with PEG and PDMA-*r*-HPA as side chains, respectively, were also synthesized as controls. The absorption spectra of these SPAs were similar, as all of them had the same SP backbones (Fig. 5b). Dynamic light scattering (DLS) measurement showed that all SPAs had hydrodynamic sizes of around 35 nm at room temperature. Upon heating, the hydrodynamic sizes of SPA16 and SPA17 dramatically increased, while that of SPA15 remained unchanged (Fig. 5c). This phenomenon can be attributed to the thermo-responsive feature of PDMA-*r*-HPA, enabling SPA16 and SPA17 to become more hydrophobic at high temperatures. The lower critical solution temperatures (LCSTs) of SPA16 and SPA17 were determined to be 42 °C and 48 °C, respectively.

The photothermal and PA properties of SPAs were then studied. Upon 808 nm laser irradiation, the maximum photothermal temperatures of SPA15 and SPA17 were 55 °C and 60 °C, respectively (Fig. 5d). The PA intensity of SPA15 showed no difference with or without laser irradiation at different concentrations. In contrast, at almost all concentrations studied, the PA intensities of SPA17 with laser irradiation were higher than those without laser irradiation (Fig. 5e). This phenomenon can be explained by the aggregation of SPA17 at high temperature induced by laser irradiation, leading to promoted heat dissipation within nanoparticles and enhanced PA intensity.

Cytotoxicity study indicated that both SPA15 and SPA17 were non-cytotoxic to 4T1 cells even at a concentration of 100 μg mL^{-1}. SPA15 and SPA17 were then applied for *in vivo* PA imaging of tumor. After i.v. injection of SPA15 or SPA17, the PA signal in the tumor area gradually increased. For both SPA15 and SPA17-injected mice, the PA intensity in the tumor area reached a maximum at 24 h post-injection. To study the *in vivo* thermo-responsive properties of SPAs, at 24 h post-injection, the tumor areas of SPA15 and SPA17-injected mice were irradiated under an 808 nm laser for 1 min (Fig. 5f). For SPA15-injected mice, the PA intensity in the tumor site remained almost the same before and after laser irradiation. In contrast, the PA intensity in the tumor site of SPA17-injected mice after irradiation was 1.37-fold higher than that before irradiation (Fig. 5g).

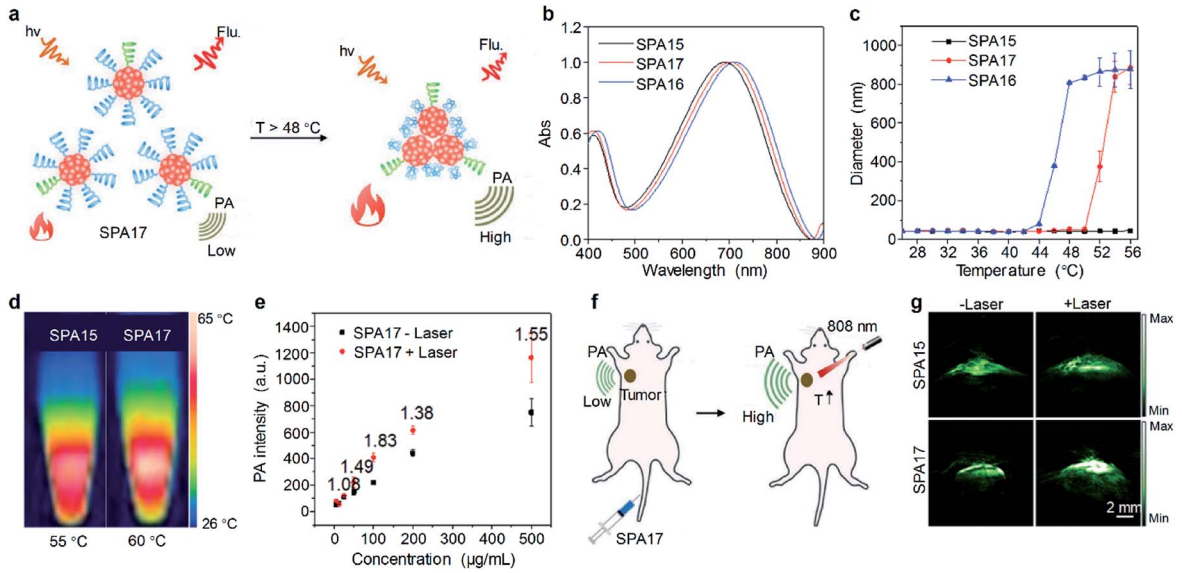

Fig. 5 (a) Schematic illustration of the heat-amplified PA signal of SPA17. (b) Absorption spectra of SPAs. (c) DLS of SPAs as a function of temperature in PBS (pH 7.4). (d) Thermal images of SPA15 and SPA17 at their respective maximum temperatures. (e) PA intensity of SPA17 as a function of concentration with or without 808 nm laser irradiation. (f) Schematic illustration of amplified PA imaging in the tumor site of SPA17-treated mice. (g) Representative PA images of tumor from living mice i.v. injected with SPA15 or SPA17 at 24 h post-injection with or without 808 nm laser irradiation. The error bars represent standard deviations of three separate measurements. Adapted from ref. 102. Copyright© 2019 Wiley-VCH Verlag GmbH & Co. KGaA, Weinheim.

These data demonstrated the advantage of thermo-responsive SPA17 in PA imaging of tumor.

4. Cancer phototheranostics

Phototheranostics which combines optical imaging with cancer therapy has gained tremendous attention in the field of cancer imaging and therapy.[103] A facile approach to design SPA-based theranostics is to use SPAs directly, as most SPAs can be used as both optical imaging and phototherapeutic agents.[104] In addition, hydrophobic drugs can be encapsulated into SPAs or conjugated onto the side chains of SPAs to give drug-loaded or -conjugated SPAs, respectively, for combination therapy. To minimize the side effects of conjugated drugs and achieve precise treatment, prodrug-conjugated SPAs can be developed to release activated drugs in the designated site under light excitation. Similarly, DNA-loaded SPAs for light-controlled remote gene regulation have also been developed (Fig. 6).

The chemical structures of SPAs for phototheranostics are shown in Schemes 3 and 4. Different from SPAs for imaging only, the side chains of SPAs for phototheranostics are not only hydrophilic moieties (SPA18-23 and SPA26), but also prodrugs (SPA27, 29, and 31), functional groups (SPA24, 25, and 30), photo-responsive groups (SPA28), and gene carriers (SPA32-34). As PCPDTBT has shown both satisfactory NIR fluorescence and PA signals as well as good PDT and PTT efficacy, numerous phototheranostic systems are designed based on it (Scheme 4). The variation of side chains endows SPAs with multi-functionality for chemotherapy, immunotherapy and gene delivery. The nanoparticles formed from SPAs for photo-theranostics usually had a larger hydrodynamic size than SPAs for imaging only, which can be attributed to the encapsulated or conjugated hydrophobic drugs. The size of such photo-theranostic SPA nanoparticles ranged from tens of nanometers

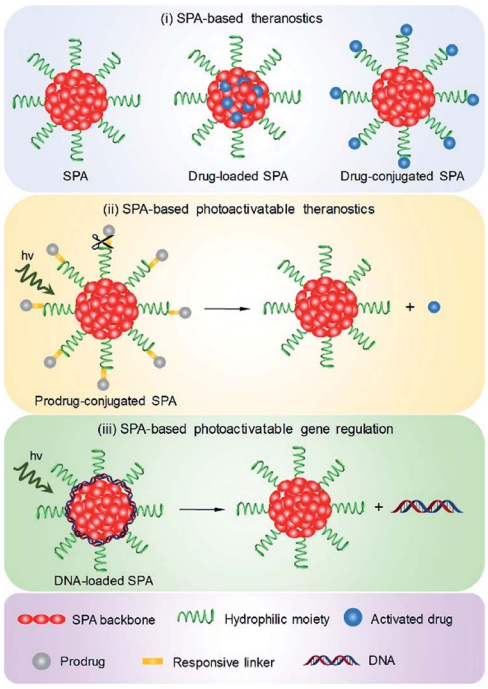

Fig. 6 Design strategies for SPA-based phototheranostics, including (i) SPAs, drug-loaded SPAs and drug-conjugated SPAs for PDT, PTT and combination therapy; (ii) prodrug-conjugated SPAs for photo-activatable drug delivery; (iii) DNA-loaded SPAs for photoactivatable gene regulation.

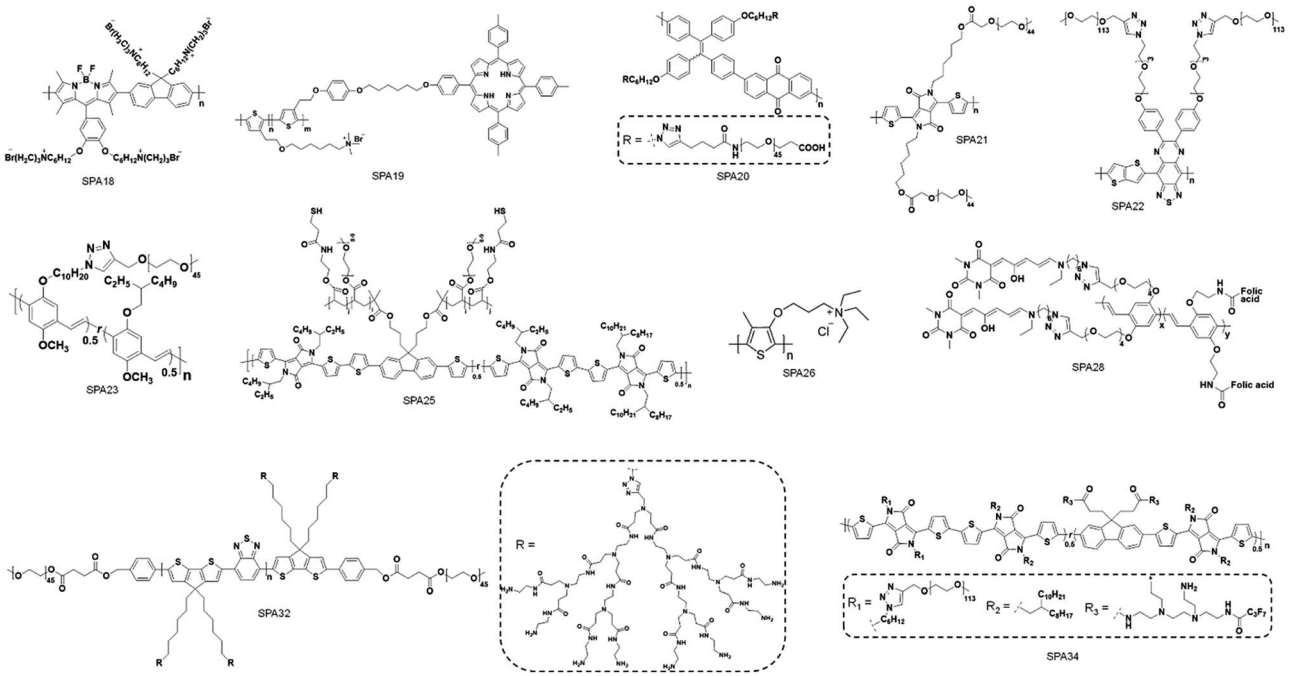

Scheme 3 Chemical structures of SPAs for phototheranostics.

to hundreds of nanometers, and the largest size can reach 350 nm (SPA19).

4.1. Imaging-guided PDT and PTT

Early studies of SPAs for phototheranostics mainly focus on *in vitro* cell imaging and therapy. SPA18 with quaternary ammonium salts as side chains was synthesized by Wang *et al.* for fluorescence cell imaging and *in vitro* PDT.[105] The same research group also developed SPA19 grafted with porphyrin as the photosensitizer and quaternary ammonium salts for *in vitro* phototheranostics.[106] Liu *et al.* designed SPA20 containing aggregation-induced emission units tetraphenylethylene for fluorescence imaging-guided cancer cell ablation.[107] SPA20 had NIR emission with good PDT efficacy. To develop SPAs suitable for *in vivo* studies, Dong *et al.* synthesized SPA21 with polydiketopyrrolopyrrole as the backbone. The low bandgap of polydiketopyrrolopyrrole endowed SPA21 with NIR absorption at wavelengths longer than 700 nm. SPA21 can be applied for *in vivo* PA imaging-guided PDT and PTT.[108]

NIR-II PA imaging that utilizes a laser longer than 1000 nm as the excitation source has deeper tissue penetration than conventional PA imaging.[109] Bian *et al.* synthesized SPA22 for NIR-II PA imaging-guided PTT.[110] SPA22 was composed of a NIR-II-absorbing semiconducting polymer backbone and PEG side chains. SPA22 had a board absorption peak ranging from 600 to

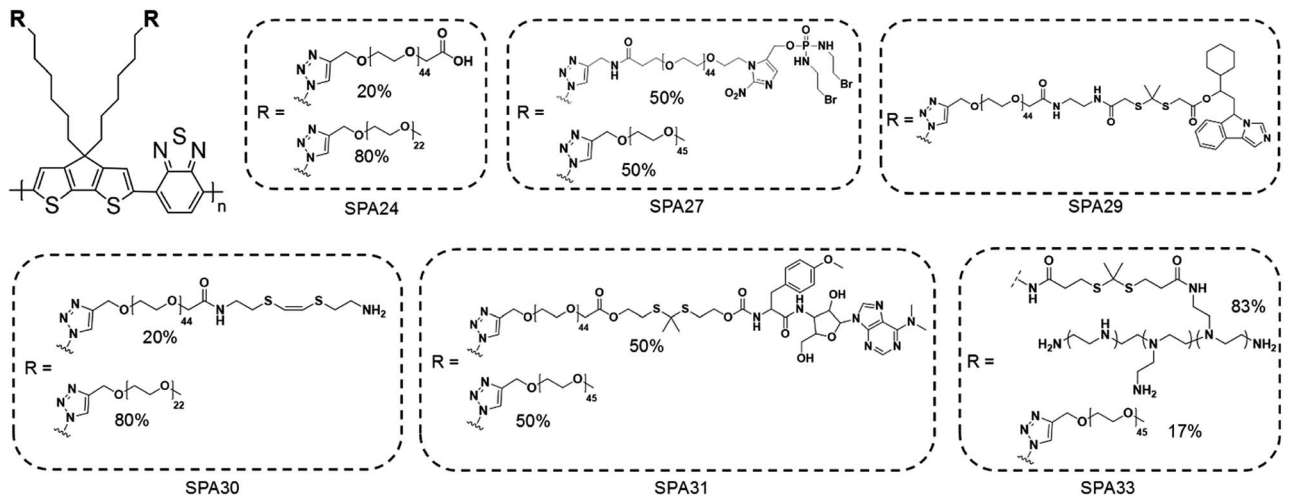

Scheme 4 Chemical structures of PCPDTBT-based SPAs for phototheranostics.

1400 nm, and the highest absorption was near 1064 nm which was suitable for NIR-II PA imaging (Fig. 7a). The PA intensities at 1064 nm linearly correlated with the concentration of SPA22, indicating its feasibility of quantification study. In addition, SPA22 also showed good PCE under 1064 nm laser irradiation, and the highest photothermal temperature can reach 91.5 °C. The penetration depth of PA imaging was then studied. For PA signals at both 820 and 1064 nm, they decreased gradually with increasing thickness of covered chicken breast tissue (Fig. 7b). However, the SBR of the PA signal at 1064 nm was higher than that at 820 nm at each thickness of the tissue, indicating a higher tissue penetration depth for PA imaging at 1064 nm than at 820 nm. No cytotoxicity was observed for SPA22 at a high concentration of 200 μg mL^{-1}, indicating its good *in vitro* biocompatibility. SPA22 was then applied for *in vivo* NIR-II PA imaging. After i.v. injection of SPA22, the PA signal at the tumor area gradually increased and reached a maximum at 6 h post-injection with an intensity ~5.36-fold higher than that before injection (Fig. 7c). Owing to the high PCE, SPA22 can also be used as an *in vivo* PTT agent. The tumor temperature of SPA22-treated mice gradually increased under 1064 nm laser irradiation and reached 58.2 °C after continuous irradiation for 5 min (Fig. 7d). In contrast, the tumor temperature only had little increase for PBS-treated mice under the same laser irradiation conditions. These results indicated that SPA22 was a good phototheranostic agent for NIR-II PA imaging-guided PTT.

Besides fluorescence and PA imaging, afterglow imaging can also be utilized for phototheranostics. SPA23 with PPV as the backbone was synthesized for real-time temperature monitoring during PTT by afterglow imaging.[43] SPA23 was co-assembled with a PTT agent poly(silolodithiophene-*alt*-diketopyrrolopyrrole) in the presence of DSPE-PEG to form a phototheranostic system. Because the intensity of the afterglow signal was correlated with temperature, the tumor temperature during the PTT process can be real-time monitored by the afterglow signal of SPA23.

Tumor extracellular-matrix (ECM) protein is the main barrier for the penetration of nanomedicines into tumor sites. Numerous studies have been conducted to overcome such a problem.[111] As collagen is the most abundant tumor ECM protein, the digestion of collagen around tumor is a feasible way to enhance the penetration of nanomedicines.[112] Thus, a bromelain (Bro)-conjugated SPA, SPA24-Bro, was synthesized by an amidation reaction between carboxyl group-grafted SPA24 and Bro (Fig. 7e).[113] Bro is a protease that digests collagen at around 45 °C.[114] Upon laser irradiation, the local temperature of SPA24 will increase, and then Bro will be activated to digest collagen around tumor tissue, thus improving the penetration of nanomedicines into the tumor. The highest photothermal temperature of SPA24-Bro was 52.1 °C, which was high enough to activate Bro. The enzymatic activity of SPA24-Bro was approximately 1510.9 GDU g^{-1} under laser irradiation, which was 2.3-fold higher than that without irradiation (Fig. 7f), demonstrating the activation of Bro under laser irradiation.

SPA24-Bro was then applied for *in vivo* phototheranostics, and SPA24 was used as a control. After i.v. injection of SPA24-Bro or SPA24, the tumors of mice were irradiated under a laser with low energy (0.2 W cm^{-2}) to activate Bro at t = 1, 3, 5 h post-injection. Fluorescence imaging indicated that the fluorescence signal in the tumor area for SPA24-Bro-injected mice reached a maximum at t = 6 h post-injection, and the signal intensity was 1.4-fold higher than that of other groups at the same time point (Fig. 7g). This result indicated that laser irradiation could enhance the tumor accumulation of SPA24-

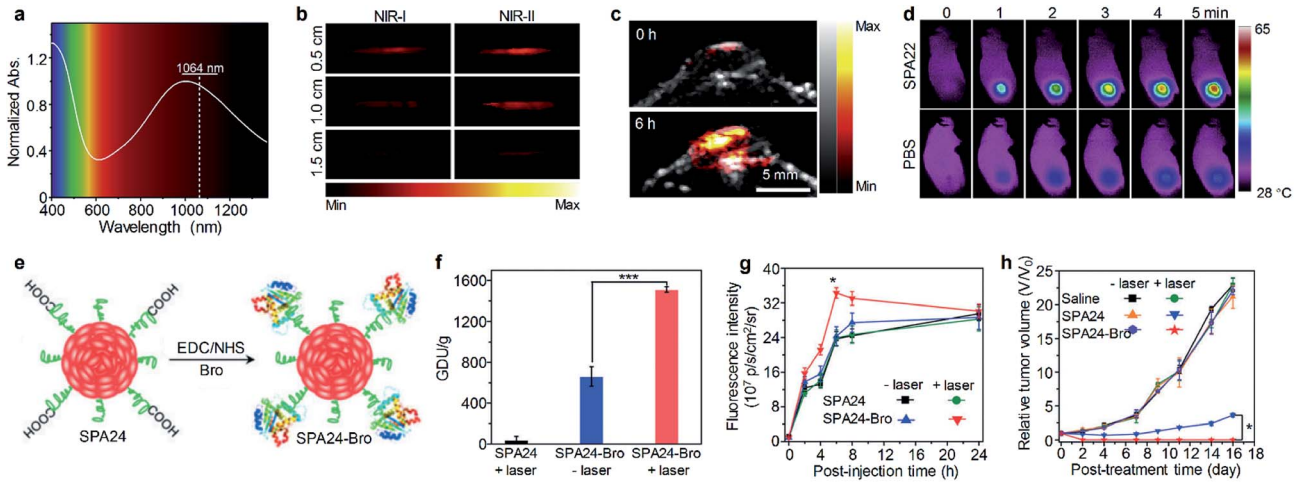

Fig. 7 (a) Absorption spectrum of SPA22 in aqueous solution. (b) PA images of SPA22 solution covered by chicken breast tissue of different thickness. For each depth, images were recorded under both NIR-I (820 nm) and NIR-II (1064 nm) lasers. (c) Representative NIR-II PA images of the tumor area from living mice treated with SPA22 at 0 and 6 h post-injection. (d) Infrared thermal images of mice treated with SPA22 or PBS at different laser irradiation times. (e) Schematic illustration for the synthesis of SPA24-Bro. (f) Gelatin digestion activity (in GDU) of SPA24 and SPA24-Bro with or without laser irradiation. (g) Fluorescence intensity of the tumor area as a function of post-injection time of SPA24 or SPA24-Bro. (h) Tumor growth curve of different groups. The error bars represent the standard deviations of three separate measurements (n = 3). *Statistically significant difference (p < 0.05, n = 3). ***Statistically significant difference (p < 0.001, n = 3). Adapted from ref. 110 and 113. Copyright© 2020 Elsevier and 2018 Wiley-VCH Verlag GmbH & Co. KGaA, Weinheim.

Bro, which can be attributed to the digestion of collagen around the tumor tissue. Because of the enhanced tumor accumulation, the SPA24-Bro-injected mice with laser irradiation showed the best PTT efficacy among all the treatments (Fig. 7h). Moreover, SPA24-Bro-induced PTT showed no damage to the major organs of mice, demonstrating the safety of such a treatment.

Another example of enhanced PTT was given by Chen's group. They synthesized SPA25 for pH/GSH-responsive enhanced PTT.[115] SPA25 was composed of a NIR-absorbing SP backbone with PEG and thiol groups as side chains. SPA25 can incorporate polyoxometalate clusters (POM) to form SPA25@POM. The formed SPA25@POM may aggregate at acidic pH and in the presence of GSH, leading to enhanced PA intensity and PTT efficacy of SPA25@POM. With such a feature, SPA25@POM can be applied for *in vivo* PA imaging-guided enhanced PTT.

4.2. Imaging-guided combination therapy

Combination therapy which combines several therapeutic methods into one system may overcome the disadvantages of individual methods, thus providing improved therapeutic efficiency.[116] A facile approach to endow SPAs with the ability for combination therapy is encapsulating hydrophobic anticancer drugs into SPAs. SPA15 can be used as a nanocarrier to load doxorubicin (DOX) *via* hydrophobic and π–π interaction, forming a DOX-loaded SPA (DSPA).[117] Owing to the NIR absorption and emission of SPA15, the DSPA can be applied for *in vivo* fluorescence/PA imaging-guided PDT/PTT combined chemotherapy.

Enhancing the penetration of anticancer drugs into cancer cells is one of the effective methods to improve anticancer efficiency. Wang *et al.* designed SPA26-based soft particles to enhance the permeability of cancer cell membranes, thus improving the diffusion of DOX into cells.[118] The soft particles were composed of a quaternary ammonium salt-grafted SPA, SPA26, and a gemini surfactant SDHC. Such soft particles can easily incorporate into the cell membrane owing to the strong self-assembly ability of SDHC. Upon light irradiation, SPA26 may generate singlet oxygen and other ROS to oxidize the unsaturated phospholipid molecules, thus increasing the permeability of cell membranes and the penetration of DOX into cells (Fig. 8a). The cellular uptake of DOX under different treatments was then studied using confocal fluorescence imaging. Without light irradiation, the soft particle-treated cells exhibited higher DOX accumulation than SPA26-treated cells, indicating enhanced cell membrane permeability with SDHC. After light irradiation, the DOX accumulation in the SPA26-treated cells markedly increases, which can be attributed to the oxidation of the cell membrane by ROS generated from SPA26. Unsurprisingly, the highest DOX accumulation was observed in soft particle-treated cells with light irradiation, indicating the highest cell membrane permeability among all the treatments (Fig. 8b). Cy5-modified SDHC (SDHC-Cy5) was then synthesized to confirm the mechanism of enhancing cell

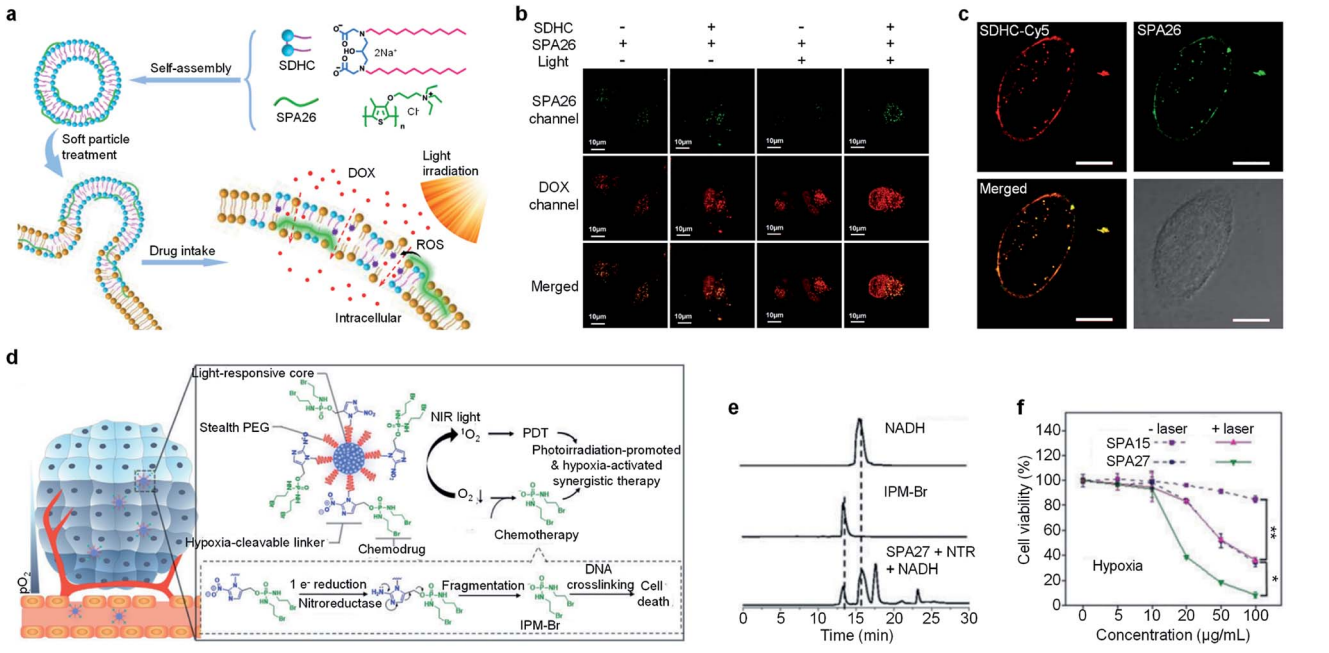

Fig. 8 (a) Schematic illustration for soft particle-mediated enhanced anticancer therapy. (b) Confocal fluorescence images of DOX and SPA26 in MCF-7 cells after different treatments. (c) Confocal fluorescence images of SDHC-Cy5 and SPA26 in MCF-7 cells after incubation for 1 h. The scale bars represent 10 μm. Cell viability of A549 and HeLa cells incubated with different concentrations of SPA26. (d) Schematic illustration of SPA27 for hypoxia-activated synergistic PDT and chemotherapy. (e) HPLC profiles of NADH, IPM-Br and SPA27 incubated with NTR and NADH under anaerobic conditions for 6 h. (f) Cell viability of 4T1 cells treated with SPA15 or SPA27 at different concentrations under hypoxic conditions with or without laser irradiation. Error bars represent the standard deviations of three different measurements ($n = 3$). *Statistically significant difference ($p < 0.05$, $n = 3$). **Statistically significant difference ($p < 0.01$, $n = 3$). Adapted from ref. 118 and 120. Copyright© 2018 American Chemical Society and 2019 Wiley-VCH Verlag GmbH & Co. KGaA, Weinheim.

permeability by soft particles. Confocal fluorescence imaging indicated that both SDHC-Cy5 and SPA26 were mainly distributed on the cell membrane after incubation with MCF-7 cells for 1 h (Fig. 8c). In addition, small changes in the zeta potential of cells were observed after incubation with soft particles, which also verified the incorporation of soft particles with the cell membrane.

One of the limitations of PDT is the lack of oxygen in the hypoxic tumor tissue, which significantly suppresses the efficacy of PDT.[119] To overcome such a limitation, a hypoxia-responsive prodrug-conjugated SPA (SPA27) was developed.[120] PCPDTBT with satisfactory PDT efficiency was utilized as the backbone of SPA27. The side chains of SPA27 were PEG, and 50% of PEG chains were conjugated with a bromoisophosphoramide mustard intermediate (IPM-Br) *via* a nitroreductase (NTR)-responsive linker. Upon the PDT process, the oxygen in the tumor site will be transferred into singlet oxygen. Meanwhile, the oxygen depletion process induced the generation of NTR in the tumor tissue, further initiating the release of IPM-Br. As such, SPA27 can integrate PDT with hypoxic-responsive chemotherapy for synergistic combination therapy (Fig. 8d).

The singlet oxygen generation efficiency for SPA27 was determined to be 3.75% under 808 nm laser irradiation, which was 18-fold higher than that of indocyanine green (ICG) (0.2%). The release profile of SPA27 was studied by HPLC. After incubating SPA27 with NTR and nicotinamide adenine dinucleotide (NADH) under anaerobic conditions for 6 h, the resulting solution was analyzed by HPLC. An elution peak at 12.82 min which can be assigned to the peak of IPM-Br was observed, indicating the release of IPM-Br from SPA27 (Fig. 8e). Cytotoxicity studies under normoxic and hypoxic conditions were then conducted with SPA15 as the control. Under normoxic conditions, the cell viability of SPA27- or SPA15-treated cells under laser irradiation was comparable, which indicates that the prodrug on SPA27 was not activated. In contrast, under hypoxic conditions without laser irradiation, the cell viability of SPA27-treated cells was 34.1% at a concentration of 100 μg mL^{-1}, much lower than that under normoxic conditions (84.8%). In addition, the cell viability further decreased to 8.3% under laser irradiation (Fig. 8f). These results showed that IPM-Br can be released under hypoxic conditions and had a significant anticancer effect. SPA27 was then utilized for *in vivo* fluorescence imaging of tumor, and it had the highest accumulation in tumor compared with other major organs. *In vivo* therapeutic study indicated that SPA27-integrated PDT and hypoxic-responsive chemotherapy had a better therapeutic efficiency than SPA27 without laser irradiation and PDT induced by SPA15.

4.3. Light-triggered drug delivery

Remotely controlling drug release in the designated disease site is important in cancer therapy, as it can not only improve the therapeutic efficiency but also minimize the side effect of drugs.[121,122] Among a variety of mediums for remote control, light has shown its unique advantages such as high spatio-temporal resolution and low toxicity.[123] Wang *et al.* developed SPA28 with photo-responsive hydrophobic side chains for light-triggered drug release.[124] Upon 550 nm light irradiation, such hydrophobic side chains may become hydrophilic, leading to the dissociation of nanoparticles and the release of encapsulated anticancer drugs.

Cancer immunotherapy which stimulates the immune system to attack cancer cells has shown great potential in cancer therapy.[125,126] However, cancer immunotherapy usually has the risk of immune-related adverse events because of the accumulation and activation of immunotherapeutic agents in normal tissues.[127] To overcome this disadvantage, a photoactivatable pro-nanostimulant SPA29 was designed and synthesized.[128] SPA29 was composed of a PCPDTBT backbone grafted with PEG-conjugated NLG919, an immunostimulant, through a singlet oxygen-cleavable linker. Upon NIR laser irradiation, SPA29 can simultaneously generate heat and singlet oxygen for PTT and PDT, respectively, causing the release of tumor-associated antigens. The generated singlet oxygen can also cleave the linker between NLG919 and PEG, releasing activated NLG919. NLG919 can promote the activation and proliferation of effector T cells and suppress the regulatory T (Treg) cells. Therefore, SPA29 synergistically integrated phototherapy with immune checkpoint blockade therapy against both primary tumor and distant metastatic tumor (Fig. 9a).

SPA29 had similar absorption and emission spectra to SPA15 (Fig. 9b). The singlet oxygen generation of SPA29 under laser irradiation was confirmed using SOSG as an indicator. The release of NLG919 from SPA29 under laser irradiation was studied by HPLC. After 808 nm laser irradiation for 15 min, an elution peak at 18.1 min was observed for SPA29, which was consistent with the elution time of NLG919, indicating the release of NLG919 (Fig. 9c). Confocal fluorescence imaging indicated that SPA29 can be efficiently internalized into cells. NLG919 has been demonstrated to inhibit the activity of indoleamine 2,3-dioxygenase (IDO), thus suppressing the generation of kynurenine (Kyn).[129] Therefore, the inhibition of IDO by SPA29 under laser irradiation was then examined by determining the Kyn content. The Kyn content in the SPA29-treated group with 808 nm laser irradiation was 4.5-fold lower than that in the control group. In addition, such a reduction was not observed in the SPA15-treated group and SPA29-treated group without laser irradiation (Fig. 9d). These results indicated that SPA29 can inhibit IDO under laser irradiation because of the release of NLG919.

In vivo phototherapeutic efficiency of SPA29 was then studied. *In vivo* NIR fluorescence imaging indicated that the highest accumulation of SPA29 in tumor was at $t = 24$ h post-injection. Phototherapy was conducted at the same time point and showed good therapeutic efficiency for SPA29-injected mice. The generation of singlet oxygen in tumor tissue was confirmed by confocal fluorescence imaging (Fig. 9e). In addition, SPA29-induced phototherapy also showed the inhibition of distant tumor and lung metastasis, which can be attributed to the immune checkpoint blockade therapy initiated by NLG919. Such immune therapy was confirmed by the increase of $CD3^+CD8^+$ T cells and the decrease of Treg cells in the distant tumor (Fig. 9f and g). In addition, vital blood parameters, the serum liver function and kidney function indicators of mice

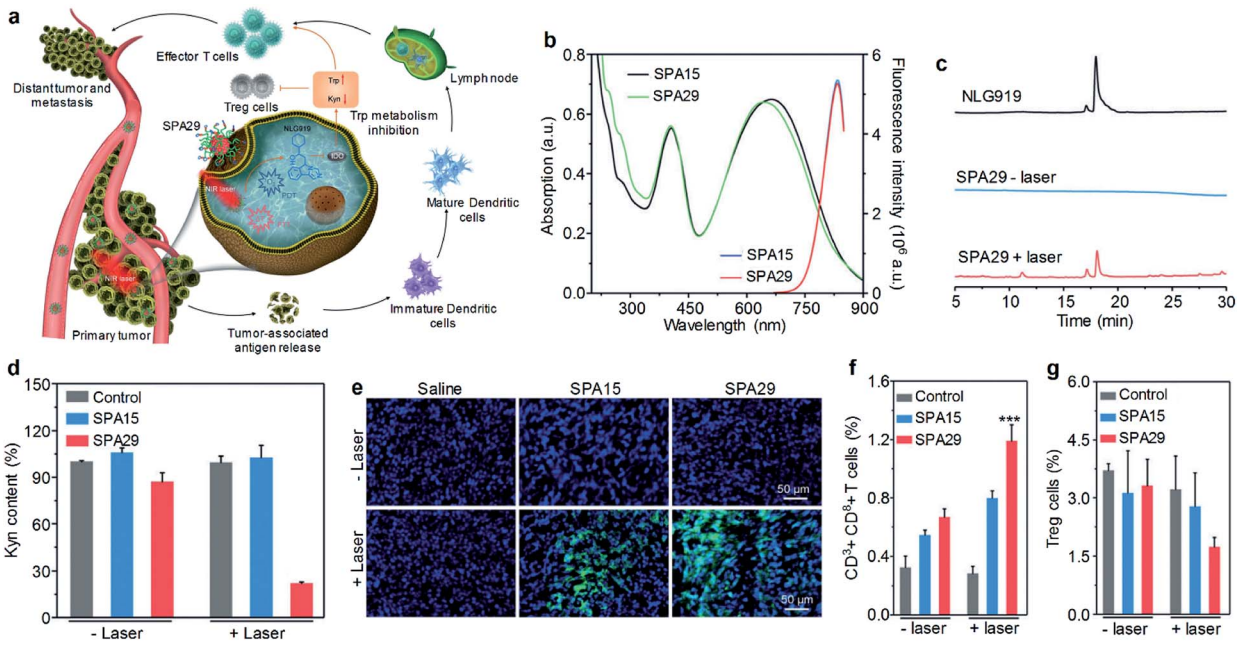

Fig. 9 (a) Schematic illustration for photoactivation of SPA29 for the combination of phototherapy and checkpoint blockade immunotherapy. (b) Absorption and fluorescence spectra of SPA15 and SPA29. Black and green lines are absorption spectra and blue and red lines are fluorescence spectra. (c) HPLC profiles for NLG919 and SPA29 with or without 808 nm laser irradiation for 15 min. (d) Relative Kyn content in the cell culture medium treated with SPA15 or SPA29 with or without laser irradiation for 6 min. Error bars represent the standard deviations of three different measurements ($n = 3$). (e) Confocal fluorescence images of primary tumors from saline, SPA15 or SPA29-injected mice with or without laser irradiation for 6 min. Blue fluorescence shows the nucleus of cancer cells stained with DAPI. Green fluorescence is the signal of SOSG. Population of $CD3^+CD8^+$ T cells (f) and Treg cells (g) in distant tumors. Error bars represent the standard deviations of five different measurements ($n = 5$). ***Statistically significant difference ($p < 0.001$, $n = 5$). Adapted from ref. 128. Copyright© 2019 Wiley-VCH Verlag GmbH & Co. KGaA, Weinheim.

remained at normal levels after treatment, indicating the minimal size effect of treatment.

Suppressing cancer metastasis is important, as metastasis is one of the major causes of death from cancer.[130] Therefore, two PCPDTBT-based SPAs (SPA30 and SPA31) were designed for the inhibition of lung metastasis. The side chain of SPA30 was modified by a singlet oxygen-cleavable linker with amino groups which can conjugate a proenzyme derived from cytotoxic ribonuclease A (RNase A).[131] Such a proenzyme can be activated in the presence of H_2O_2, and it can be released from SPA30 under laser irradiation *via* the cleavage of the singlet oxygen-sensitive linker between SPA30 and the proenzyme. Thus, the proenzyme-conjugated SPA30 can precisely deliver and activate RNase A in the tumor site under laser irradiation. Combined with phototherapy, the primary tumor can be ablated and lung metastasis can also be inhibited. SPA31 was covalently linked to a blockader molecule, puromycin, which can terminate protein synthesis and induce cell death.[132] Similar to SPA30, the conjugated puromycin can only be activated in the tumor tissue under laser irradiation, thus killing cancer cells and inhibiting metastasis.

4.4. Light-triggered gene regulation

Gene therapy has shown great promise in the treatment of genetic diseases and cancer.[133] However, the off-target gene expression in normal tissue may lead to severe side effects during the therapeutic process.[134] Thus, the development of delivery systems for precisely regulated gene expression in the designated disease site is highly demanded. Light has been demonstrated as an ideal inducer for gene expression because of its low cost, high spatial resolution and low toxicity.[135] Consequently, a photo-responsive gene delivery nanoplatform was developed using SPA32 with cationic third-generation polyamidoamine (PAMAM) as the side chain.[136] SPA32 can load a heat shock promoter (HSP70)-regulated gene which can be activated by a photothermal signal. After delivering the gene into the cell nucleus, the photothermal signal induced by SPA32 may trigger the heat shock factor (HSF) monomer to transfer into HSF trimers. The HSF trimers can translocate to the nucleus and bind to the heat shock element in HSP70 to activate transcription.

CRISPR/Cas9 is one of the most efficient gene editing methods and has been widely used in the research. However, it still faces the issue of off-target mutagenesis.[137] To improve the selectivity of CRISPR/Cas9-based gene editing, a photo-responsive nanotransducer (SPA33) was prepared.[138] SPA33 had low molecular polyethylenimine (PEI) as the side chain which can bind CRISPR "all-in-one" plasmid containing the genes of Cas9 and sgRNA. After being internalized into cells, the SPA33/CRISPR nanocomplex can selectively release the CRISPR all-in-one plasmid under laser irradiation *via* the cleavage of the singlet oxygen responsive bond. The released plasmid then entered the nucleus of cells and initiated the gene editing

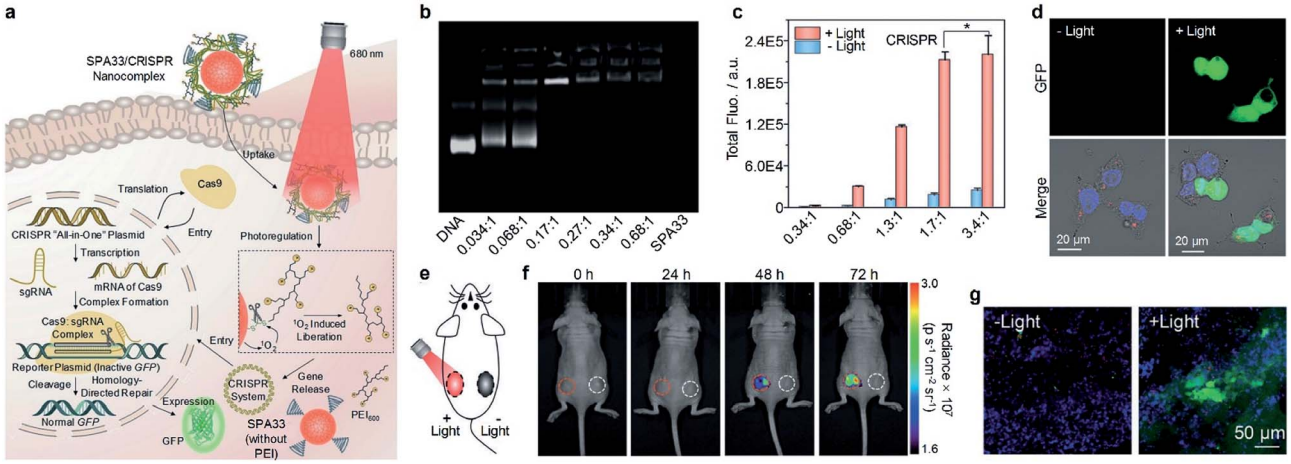

Fig. 10 (a) Schematic illustration of SPA33-mediated delivery and photoregulation of CRISPR/Cas9 gene editing. (b) Agarose gel electrophoresis of DNA, SPA33 and DNA/SPA33 complexes at different N/P ratios. (c) Total fluorescence of GFP for SPA33/CRISPR complexes at different N/P ratios with or without 680 nm laser irradiation. (d) Confocal fluorescence images of SPA33/CRISPR-transfected cells with or without 680 nm laser irradiation. (e) Schematic illustration of laser irradiation for living mice. (f) Fluorescence images of mice at different post-irradiation times with (red circles) or without (white circles) 680 nm laser irradiation. The red/white circles indicate the regions with subcutaneously implanted Matrigel mixed HeLa cell pellets transfected with SPA33/CRISPR with/without laser irradiation. (g) Confocal fluorescence images of Matrigel mixed cell pellet slices from mice with or without laser irradiation at $t = 72$ h post-treatment. The blue, green and red fluorescence indicate nuclei, GFP and SPA33, respectively. Error bars represent the standard deviations of three different measurements. *No statistically significant difference. Adapted from ref. 138. Copyright© 2019 Wiley-VCH Verlag GmbH & Co. KGaA, Weinheim.

process, resulting in the expression of green fluorescent protein (GFP) (Fig. 10a). To study the loading capability of SPA33 for plasmids, the pCMV-GFP plasmid was used to incorporate with SPA33. Agarose gel electrophoresis results indicated that all the plasmid can be loaded onto SPA33 at a low nitrogen to phosphate ratio (N/P) of 0.17 : 1 (Fig. 10b). At such a N/P ratio, 82.8% of the loaded plasmids can be released after laser irradiation, while no release was observed without irradiation. However, the transfection efficacy at such a N/P ratio in HeLa cells was not high enough, and a higher N/P ratio should be used for gene editing in living cells. For SPA33/CRISPR complex-treated HeLa cells, the total GFP fluorescence in laser-irradiated cells increased with increasing N/P ratio and reached the maximum at a N/P ratio of 1.7 : 1 (Fig. 10c). This result was also confirmed by confocal fluorescence images, in which the laser-irradiated cells showed obvious green fluorescence (Fig. 10d). These data demonstrated that the SPA33/CRISPR complex can effectively induce CRISPR/Cas9 gene editing in living cells.

As the N/P ratio of 1.7 : 1 showed the highest fluorescence in cell studies, this ratio was chosen for the subsequent *in vivo* gene editing studies. Matrigel was used to mix with HeLa cells transfected with the SPA33/CRISPR complex, and the resulting mixtures were subcutaneously injected into the back of mice at two sides (Fig. 10e). The left side was then exposed to a 680 nm laser for 20 min, and the fluorescence images of mice were captured at the designated time points. The green fluorescence signal at the left side increased gradually over time, and the intensity was 1.2-, 1.5- and 1.8-fold higher than that at the right side without laser irradiation at $t = 24$, 48 and 72 h post-injection, respectively (Fig. 10f). Confocal fluorescence images of Matrigel slices taken from the mice also indicated that the laser-irradiated Matrigel slices showed strong green fluorescence, while the non-irradiated slices showed almost no green fluorescence signal (Fig. 10g). These results demonstrated the feasibility of *in vivo* CRISPR/Cas9 gene editing at the designated position by the SPA33/CRISPR complex.

Another study for the regulation of CRISPR/Cas9 gene editing by SPA was conducted by Chen *et al.*[139] They synthesized SPA34 with fluorinated polyethylenimine as the side chain to load CRISPR/Cas9 plasmids. A NIR-II fluorescent SP was used as the backbone of SPA34 so that the location of SPA34 can be real-time monitored by NIR-II fluorescence imaging, and the quantum yield of SPA34 was 0.23%. In addition, dexamethasone which can dilate the nuclear pore was encapsulated into the nanocomplex. Upon laser irradiation, the CRISPR/Cas9 plasmids and dexamethasone were released from SPA34. With the help of dexamethasone, CRISPR/Cas9 plasmids can be easily translocated to the cell nucleus for gene editing. However, SPA34 used photothermal heat to increase molecule movement and there was no thermal-responsive linker between PEI brushes and the polymer backbone to precisely control the release of plasmid as SPA33 did.

5. Conclusion and outlook

SPAs have been demonstrated to be a multi-functional platform for imaging-guided cancer therapy. Because of their amphiphilic feature, SPAs can directly self-assemble in aqueous solution without the help of other amphiphilic copolymers. Such an advantage endows SPAs with good stability and improved biodistribution profiles in cancer theranostics. Our results showed that no cytotoxicity was observed even at a concentration as high as 200 μg mL^{-1} for SPAs. Also, no damage was observed for the major organs of mice treated with

SPAs at a dosage of 2 mg kg^{-1}. All of these results indicated the good biocompatibility of SPAs. Owing to the unique optical properties of SPA backbones, SPAs are good candidates for optical imaging. PEG-grafted SPAs with improved fluorescence or PA properties can be applied for fluorescence and PA imaging of cancer cells or tumors. Besides conventional fluorescence and PA imaging, SPAs with PPV as the backbone can be used for afterglow tumor imaging with ultrahigh sensitivity. To overcome the disadvantages of optical imaging such as low tissue penetration, SPAs integrated with Gd^{3+} ions or ^{99m}Tc complexes can be utilized for multimodal imaging. SPAs can also be developed into activatable imaging nanoprobes by using stimuli-responsive side chains or ROS-responsive backbones.

Taking advantage of the broad applications of SPAs in cancer imaging, SPAs can also be applied for imaging-guided cancer therapy. As most SPs have either good singlet oxygen quantum yield or photothermal conversion efficiency, SPAs themselves can be used for imaging-guided phototherapy. In addition, anticancer drugs can be encapsulated into or conjugated onto SPAs to give drug-loaded or drug-conjugated SPAs, respectively, for imaging-guided combination therapy. By conjugating prodrugs onto SPAs *via* singlet oxygen-responsive groups, prodrug-conjugated SPAs can be developed. Such SPAs may only release activated drugs upon light irradiation, leading to minimal side effects with improved therapeutic efficiency. Finally, DNA can also be loaded onto SPAs with cationic side chains for light-regulated gene expression or editing.

Although SPAs have shown great promise in the field of cancer imaging and therapy, they are still in the basic research stage and several critical issues need to be resolved. Most SPAs and SPA-developed nanoplatforms have the hydrodynamic sizes of tens of nanometers or even larger, which can only be cleared out of body through hepatobiliary excretion. Thus, the long-term biosafety of SPAs is a critical issue as hepatobiliary excretion may take several weeks. Although some studies have shown the good biocompatibility of SPAs both *in vitro* and *in vivo*, the biosafety of SPAs over relatively long term is rarely studied, which is an important issue for the clinical translation of SPAs. To address this issue, the development of SPAs with biodegradability or ultrasmall size are feasible methods. Both kinds of SPAs may have a shorter metabolic duration than conventional SPAs.

Until now, some studies have focused on the development of biodegradable SPAs. However, most of them can only be degraded under harsh conditions such as ROS, and few of them can be degraded under mild physiological conditions. In addition, the unknown degradation products may also cause the issue of biosafety. SPAs with ultrasmall size (<5 nm) can be cleared out through urinary excretion. Such an excretion pathway can significantly improve the clearance efficiency. The diameter of SPAs usually correlates with two parameters, the molecular weight of the backbone and the density of hydrophilic groups such as PEG. To minimize the size of SPAs, a low molecular weight backbone and high hydrophilic group density are preferred for SPA design. Therefore, designing novel structures with such a requirement for SPAs can be one of the research focuses.

Conflicts of interest

There are no conflicts to declare.

Acknowledgements

K. P. thanks Nanyang Technological University (Start-Up grant: M4081627) and Singapore Ministry of Education Academic Research Fund Tier 1 (2017-T1-002-134-RG147/17; 2019-T1-002-045-RG125/19) and Academic Research Fund Tier 2 (MOE2018-T2-2-042) for the financial support. Q. F. thanks the National Natural Science Foundation of China (21674048) for the financial support. C. X. thanks the National Natural Science Foundation of China (61905122) and Natural Science Foundation of Jiangsu Province (BK20190735) for the financial support.

Notes and references

1 H. Chen, W. Zhang, G. Zhu, J. Xie and X. Chen, *Nat. Rev. Mater.*, 2017, **2**, 17024.
2 C. Li, *Nat. Mater.*, 2014, **13**, 110–115.
3 Y. Cai, Z. Wei, C. Song, C. Tang, W. Han and X. Dong, *Chem. Soc. Rev.*, 2019, **48**, 22–37.
4 J. Li and K. Pu, *Chem. Soc. Rev.*, 2019, **48**, 38–71.
5 Y. Jiang and K. Pu, *Acc. Chem. Res.*, 2018, **51**, 1840–1849.
6 J. F. Lovell, T. W. B. Liu, J. Chen and G. Zheng, *Chem. Rev.*, 2010, **110**, 2839–2857.
7 J. F. Lovell, C. S. Jin, E. Huynh, H. Jin, C. Kim, J. L. Rubinstein, W. C. W. Chan, W. Cao, L. V. Wang and G. Zheng, *Nat. Mater.*, 2011, **10**, 324–332.
8 J. V. Jokerst and S. S. Gambhir, *Acc. Chem. Res.*, 2011, **44**, 1050–1060.
9 J. Zhang, L. Ning, J. Huang, C. Zhang and K. Pu, *Chem. Sci.*, 2020, **11**, 618–630.
10 L. Cheng, C. Wang, L. Feng, K. Yang and Z. Liu, *Chem. Rev.*, 2014, **114**, 10869–10939.
11 K. Yang, H. Xu, L. Cheng, C. Sun, J. Wang and Z. Liu, *Adv. Mater.*, 2012, **24**, 5586–5592.
12 G. Qi, F. Hu, Kenry, L. Shi, M. Wu and B. Liu, *Angew. Chem., Int. Ed.*, 2019, **58**, 16229–16235.
13 Z. Yang, W. Fan, J. Zou, W. Tang, L. Li, L. He, Z. Shen, Z. Wang, O. Jacobson, M. A. Aronova, P. Rong, J. Song, W. Wang and X. Chen, *J. Am. Chem. Soc.*, 2019, **141**, 14687–14698.
14 S. He, C. Xie, Y. Jiang and K. Pu, *Adv. Mater.*, 2019, **31**, 1902672.
15 Z. Yang and X. Chen, *Acc. Chem. Res.*, 2019, **52**, 1245–1254.
16 Q. Wang, Y. Dai, J. Xu, J. Cai, X. Niu, L. Zhang, R. Chen, Q. Shen, W. Huang and Q. Fan, *Adv. Funct. Mater.*, 2019, **29**, 1901480.
17 C. Chen, H. Ou, R. Liu and D. Ding, *Adv. Mater.*, 2020, **32**, 1806331.
18 X. Zhen, J. Zhang, J. Huang, C. Xie, Q. Miao and K. Pu, *Angew. Chem., Int. Ed.*, 2018, **57**, 7804–7808.
19 M. Li, S. Long, Y. Kang, L. Guo, J. Wang, J. Fan, J. Du and X. Peng, *J. Am. Chem. Soc.*, 2018, **140**, 15820–15826.

20 J. Zhou, Y. Jiang, S. Hou, P. K. Upputuri, D. Wu, J. Li, P. Wang, X. Zhen, M. Pramanik, K. Pu and H. Duan, *ACS Nano*, 2018, **12**, 2643–2651.
21 R. Vankayala and K. C. Hwang, *Adv. Mater.*, 2018, **30**, 1706320.
22 H. Zhu, Z. Lai, Y. Fang, X. Zhen, C. Tan, X. Qi, D. Ding, P. Chen, H. Zhang and K. Pu, *Small*, 2017, **13**, 1604139.
23 H. Shi, R. Gu, W. Xu, H. Huang, L. Xue, W. Wang, Y. Zhang, W. Si and X. Dong, *ACS Appl. Mater. Interfaces*, 2019, **11**, 44970–44977.
24 W. Tang, W. Fan, W. Zhang, Z. Yang, L. Li, Z. Wang, Y. L. Chiang, Y. Liu, L. Deng, L. He, Z. Shen, O. Jacobson, M. A. Aronova, A. Jin, J. Xie and X. Chen, *Adv. Mater.*, 2019, **31**, 1900401.
25 K. Pu, A. J. Shuhendler, J. V. Jokerst, J. Mei, S. S. Gambhir, Z. Bao and J. Rao, *Nat. Nanotechnol.*, 2014, **9**, 233–239.
26 K. Pu, A. J. Shuhendler and J. Rao, *Angew. Chem., Int. Ed.*, 2013, **52**, 10325–10329.
27 A. De la Zerda, C. Zavaleta, S. Keren, S. Vaithilingam, S. Bodapati, Z. Liu, J. Levi, B. R. Smith, T. Ma, O. Oralkan, Z. Cheng, X. Chen, H. Dai, B. T. Khuri-Yakub and S. S. Gambhir, *Nat. Nanotechnol.*, 2008, **3**, 557–562.
28 L. Dou, Y. Liu, Z. Hong, G. Li and Y. Yang, *Chem. Rev.*, 2015, **115**, 12633–12665.
29 Q. Miao and K. Pu, *Adv. Mater.*, 2018, **30**, 1801778.
30 K. Pu, N. Chattopadhyay and J. Rao, *J. Controlled Release*, 2016, **240**, 312–322.
31 H. Zhu, Y. Fang, X. Zhen, N. Wei, Y. Gao, K. Luo, C. Xu, H. Duan, D. Ding, P. Chen and K. Pu, *Chem. Sci.*, 2016, **7**, 5118–5125.
32 Y. Jiang, J. Li, Z. Zeng, C. Xie, Y. Lyu and K. Pu, *Angew. Chem., Int. Ed.*, 2019, **58**, 8161–8165.
33 B. Guo, Z. Feng, D. Hu, S. Xu, E. Middha, Y. Pan, C. Liu, H. Zheng, J. Qian, Z. Sheng and B. Liu, *Adv. Mater.*, 2019, **31**, 1902504.
34 C. Wu, S. J. Hansen, Q. Hou, J. Yu, M. Zeigler, Y. Jin, D. R. Burnham, J. D. McNeill, J. M. Olson and D. T. Chiu, *Angew. Chem., Int. Ed.*, 2011, **50**, 3430–3434.
35 K. Pu, A. J. Shuhendler, M. P. Valta, L. Cui, M. Saar, D. M. Peehl and J. Rao, *Adv. Healthcare Mater.*, 2014, **3**, 1292–1298.
36 C. Yin, G. Wen, C. Liu, B. Yang, S. Lin, J. Huang, P. Zhao, S. H. D. Wong, K. Zhang, X. Chen, G. Li, X. Jiang, J. Huang, K. Pu, L. Wang and L. Bian, *ACS Nano*, 2018, **12**, 12201–12211.
37 Y. Jiang, P. K. Upputuri, C. Xie, Y. Lyu, L. Zhang, Q. Xiong, M. Pramanik and K. Pu, *Nano Lett.*, 2017, **17**, 4964–4969.
38 Y. Jiang, P. K. Upputuri, C. Xie, Z. Zeng, A. Sharma, X. Zhen, J. Li, J. Huang, M. Pramanik and K. Pu, *Adv. Mater.*, 2019, **31**, 1808166.
39 T. Stahl, R. Bofinger, I. Lam, K. J. Fallon, P. Johnson, O. Ogunlade, V. Vassileva, R. B. Pedley, P. C. Beard, H. C. Hailes, H. Bronstein and A. B. Tabor, *Bioconjugate Chem.*, 2017, **28**, 1734–1740.
40 Y. Lyu, Y. Fang, Q. Miao, X. Zhen, D. Ding and K. Pu, *ACS Nano*, 2016, **10**, 4472–4481.
41 B. Guo, J. Chen, N. Chen, E. Middha, S. Xu, Y. Pan, M. Wu, K. Li, C. Liu and B. Liu, *Adv. Mater.*, 2019, **31**, 1808355.
42 J. Li, J. Rao and K. Pu, *Biomaterials*, 2018, **155**, 217–235.
43 C. Xie, P. K. Upputuri, X. Zhen, M. Pramanik and K. Pu, *Biomaterials*, 2016, **119**, 1–8.
44 K. Pu, J. Mei, J. V. Jokerst, G. Hong, A. L. Antaris, N. Chattopadhyay, A. J. Shuhendler, T. Kurosawa, Y. Zhou, S. S. Gambhir, Z. Bao and J. Rao, *Adv. Mater.*, 2015, **27**, 5184–5190.
45 D. Cui, C. Xie and K. Pu, *Macromol. Rapid Commun.*, 2017, **38**, 1700125.
46 C. Yin, H. Zhu, C. Xie, L. Zhang, P. Chen, Q. Fan, W. Huang and K. Pu, *Adv. Funct. Mater.*, 2017, **27**, 1700493.
47 X. Zhen and K. Pu, *Nano Res.*, 2018, **11**, 5258–5280.
48 Q. Miao, Y. Lyu, D. Ding and K. Pu, *Adv. Mater.*, 2016, **28**, 3662–3668.
49 D. Mao, W. Wu, S. Ji, C. Chen, F. Hu, D. Kong, D. Ding and B. Liu, *Chem*, 2017, **3**, 991–1007.
50 Q. Miao, C. Xie, X. Zhen, Y. Lyu, H. Duan, X. Liu, J. V. Jokerst and K. Pu, *Nat. Biotechnol.*, 2017, **35**, 1102–1110.
51 L. Jiang, H. Bai, L. Liu, F. Lv, X. Ren and S. Wang, *Angew. Chem., Int. Ed.*, 2019, **58**, 10660–10665.
52 Y. Jiang, J. Huang, X. Zhen, Z. Zeng, J. Li, C. Xie, Q. Miao, J. Chen, P. Chen and K. Pu, *Nat. Commun.*, 2019, **10**, 2064.
53 Y. Lyu, D. Cui, J. Huang, W. Fan, Y. Miao and K. Pu, *Angew. Chem., Int. Ed.*, 2019, **58**, 4983–4987.
54 A. J. Shuhendler, K. Pu, L. Cui, J. P. Uetrecht and J. Rao, *Nat. Biotechnol.*, 2014, **32**, 373–380.
55 X. Zhen, C. Zhang, C. Xie, Q. Miao, K. L. Lim and K. Pu, *ACS Nano*, 2016, **10**, 6400–6409.
56 X. Zhen, C. Xie and K. Pu, *Angew. Chem., Int. Ed.*, 2018, **57**, 3938–3942.
57 D. Cui, J. Li, X. Zhao, K. Pu and R. Zhang, *Adv. Mater.*, 2020, **32**, 1906314.
58 H. Zhu, C. Xie, P. Chen and K. Pu, *Curr. Med. Chem.*, 2019, **26**, 1389–1405.
59 H. Zhu, Y. Fang, Q. Miao, X. Qi, D. Ding, P. Chen and K. Pu, *ACS Nano*, 2017, **11**, 8998–9009.
60 Y. Lyu, J. Zeng, Y. Jiang, X. Zhen, T. Wang, S. Qiu, X. Lou, M. Gao and K. Pu, *ACS Nano*, 2018, **12**, 1801–1810.
61 Y. Lyu, X. Zhen, Y. Miao and K. Pu, *ACS Nano*, 2017, **11**, 358–367.
62 W. Wu, D. Mao, S. Xu, Kenry, F. Hu, X. Li, D. Kong and B. Liu, *Chem*, 2018, **4**, 1937–1951.
63 T. Yang, L. Liu, Y. Deng, Z. Guo, G. Zhang, Z. Ge, H. Ke and H. Chen, *Adv. Mater.*, 2017, **29**, 1700487.
64 T. Sun, J. Dou, S. Liu, X. Wang, X. Zheng, Y. Wang, J. Pei and Z. Xie, *ACS Appl. Mater. Interfaces*, 2018, **10**, 7919–7926.
65 B. Guo, Z. Sheng, D. Hu, A. Li, S. Xu, P. N. Manghnani, C. Liu, L. Guo, H. Zheng and B. Liu, *ACS Nano*, 2017, **11**, 10124–10134.
66 G. Feng, Y. Fang, J. Liu, J. Geng, D. Ding and B. Liu, *Small*, 2017, **13**, 1602807.
67 X. Zhen, C. Xie, Y. Jiang, X. Ai, B. Xing and K. Pu, *Nano Lett.*, 2018, **18**, 1498–1505.
68 Y. Jiang, J. Li, X. Zhen, C. Xie and K. Pu, *Adv. Mater.*, 2018, **30**, 1705980.

69 H. Zhu, J. Li, X. Qi, P. Chen and K. Pu, *Nano Lett.*, 2018, **18**, 586–594.
70 B. Guo, Z. Sheng, D. Hu, C. Liu, H. Zheng and B. Liu, *Adv. Mater.*, 2018, **30**, 1802591.
71 Y. Jiang, X. Zhao, J. Huang, J. Li, P. K. Upputuri, H. Sun, X. Han, M. Pramanik, Y. Miao, H. Duan, K. Pu and R. Zhang, *Nat. Commun.*, 2020, **11**, 1857.
72 K. Li and B. Liu, *Chem. Soc. Rev.*, 2014, **43**, 6570–6597.
73 Y. Wang, L. Feng and S. Wang, *Adv. Funct. Mater.*, 2019, **29**, 1806818.
74 Z. L. Tyrrell, Y. Shen and M. Radosz, *Prog. Polym. Sci.*, 2010, **35**, 1128–1143.
75 S. C. Owen, D. P. Y. Chan and M. S. Shoichet, *Nano Today*, 2012, **7**, 53–65.
76 N. Kang, M. E. Perron, R. E. Prud'homme, Y. Zhang, G. Gaucher and J. C. Leroux, *Nano Lett.*, 2005, **5**, 315–319.
77 C. Chen, H. Ou, R. Liu and D. Ding, *Adv. Mater.*, 2020, **32**, 1806331.
78 L. Cui and J. Rao, *WIREs Nanomedicine and Nanobiotechnology*, 2017, **9**, e1418.
79 V. K. Tiwari, B. B. Mishra, K. B. Mishra, N. Mishra, A. S. Singh and X. Chen, *Chem. Rev.*, 2016, **116**, 3086–3240.
80 J. V. Frangioni, *Curr. Opin. Chem. Biol.*, 2003, **7**, 626–634.
81 C. Chen, X. Ni, H. Tian, Q. Liu, D. Guo and D. Ding, *Angew. Chem., Int. Ed.*, 2020, **59**, 10008–100012.
82 L. V. Wang and S. Hu, *Science*, 2012, **335**, 1458–1462.
83 P. Cheng, W. Chen, S. Li, S. He, Q. Miao and K. Pu, *Adv. Mater.*, 2020, **32**, 1908530.
84 C. Xie, X. Zhen, Y. Lyu and K. Pu, *Adv. Mater.*, 2017, **29**, 1703693.
85 R. Zhang, Y. Xu, Y. Zhang, H. S. Kim, A. Sharma, J. Gao, G. Yang, J. S. Kim and Y. Sun, *Chem. Sci.*, 2019, **10**, 8348–8353.
86 P. Anees, J. Joseph, S. Sreejith, N. V. Menon, Y. Kang, S. W. K. Yu, A. Ajayaghosh and Y. Zhao, *Chem. Sci.*, 2016, **7**, 4110–4116.
87 L. Zhou, J. Geng, G. Wang, J. Liu and B. Liu, *Polym. Chem.*, 2013, **4**, 5243–5251.
88 D. Cui, C. Xie, Y. Lyu, X. Zhen and K. Pu, *J. Mater. Chem. B*, 2017, **5**, 4406–4409.
89 C. Yin, X. Zhen, H. Zhao, Y. Tang, Y. Ji, Y. Lyu, Q. Fan, W. Huang and K. Pu, *ACS Appl. Mater. Interfaces*, 2017, **9**, 12332–12339.
90 C. Xie, X. Zhen, Q. Lei, R. Ni and K. Pu, *Adv. Funct. Mater.*, 2017, **27**, 1605397.
91 H. Cheng, Y. Li, B. Tang and J. Yoon, *Chem. Soc. Rev.*, 2020, **49**, 21–31.
92 X. Ni, X. Zhang, X. Duan, H. Zheng, X. Xue and D. Ding, *Nano Lett.*, 2019, **19**, 318–330.
93 C. Xie, X. Zhen, Q. Miao, Y. Lyu and K. Pu, *Adv. Mater.*, 2018, **30**, 1801331.
94 C. Xie, Y. Lyu, X. Zhen, Q. Miao and K. Pu, *ACS Appl. Bio Mater.*, 2018, **1**, 1147–1153.
95 M. Bouda, C. W. Windt, A. J. McElrone and C. R. Brodersen, *Nat. Commun.*, 2019, **10**, 5645.
96 X. Hu, Y. Tang, Y. Hu, F. Lu, X. Lu, Y. Wang, J. Li, Y. Li, Y. Ji, W. Wang, D. Ye, Q. Fan and W. Huang, *Theranostics*, 2019, **9**, 4168–4181.
97 J. T. Robinson, G. Hong, Y. Liang, B. Zhang, O. K. Yaghi and H. Dai, *J. Am. Chem. Soc.*, 2012, **134**, 10664–10669.
98 B. Jia, X. Zhang, B. Wang, M. Chen, F. Lv, S. Wang and F. Wang, *ACS Appl. Mater. Interfaces*, 2018, **10**, 6646–6651.
99 P. Cheng and K. Pu, *ACS Appl. Mater. Interfaces*, 2020, **12**, 5286–5299.
100 J. Li, C. Tian, Y. Yuan, Z. Yang, C. Yin, R. Jiang, W. Song, X. Li, X. Lu, L. Zhang, Q. Fan and W. Huang, *Macromolecules*, 2015, **48**, 1017–1025.
101 C. Yin, X. Zhen, Q. Fan, W. Huang and K. Pu, *ACS Nano*, 2017, **11**, 4174–4182.
102 D. Cui, P. Li, X. Zhen, J. Li, Y. Jiang, A. Yu, X. Hu and K. Pu, *Adv. Funct. Mater.*, 2019, **29**, 1903461.
103 K. K. Ng and G. Zheng, *Chem. Rev.*, 2015, **115**, 11012–11042.
104 C. Zhu, L. Liu, Q. Yang, F. Lv and S. Wang, *Chem. Rev.*, 2012, **112**, 4687–4735.
105 H. Chong, C. Nie, C. Zhu, Q. Yang, L. Liu, F. Lv and S. Wang, *Langmuir*, 2012, **28**, 2091–2098.
106 C. Xing, L. Liu, H. Tang, X. Feng, Q. Yang, S. Wang and G. C. Bazan, *Adv. Funct. Mater.*, 2011, **21**, 4058–4067.
107 W. Wu, G. Feng, S. Xu and B. Liu, *Macromolecules*, 2016, **49**, 5017–5025.
108 H. Shi, Y. Wang, X. Huang, P. Liang, Y. Tang, Y. Zhang, N. Fu, W. Huang and X. Dong, *J. Mater. Chem. B*, 2018, **6**, 7402–7410.
109 J. Wu, L. You, L. Lan, H. J. Lee, S. T. Chaudhry, R. Li, J. Cheng and J. Mei, *Adv. Mater.*, 2017, **29**, 1703403.
110 C. Yin, X. Li, G. Wen, B. Yang, Y. Zhang, X. Chen, P. Zhao, S. Li, R. Li, L. Wang, C. S. Lee and L. Bian, *Biomaterials*, 2020, **232**, 119684.
111 A. Zinger, L. Koren, O. Adir, M. Poley, M. Alyan, Z. Yaari, N. Noor, N. Krinsky, A. Simon, H. Gibori, M. Krayem, Y. Mumblat, S. Kasten, S. Ofir, E. Fridman, N. Milman, M. M. Lubtow, L. Liba, J. Shklover, J. Shainsky-Roitman, Y. Binenbaum, D. Hershkovitz, Z. Gil, T. Dvir, R. Luxenhofer, R. Satchi-Fainaro and A. Schroeder, *ACS Nano*, 2019, **13**, 11008–11021.
112 H. Sato, T. Takino, Y. Okada, J. Cao, A. Shinagawa, E. Yamamoto and M. Seiki, *Nature*, 1994, **370**, 61–65.
113 J. Li, C. Xie, J. Huang, Y. Jiang, Q. Miao and K. Pu, *Angew. Chem., Int. Ed.*, 2018, **57**, 3995–3998.
114 A. Parodi, S. G. Haddix, N. Taghipour, S. Scaria, F. Taraballi, A. Cevenini, I. K. Yazdi, C. Corbo, R. Palomba, S. Z. Khaled, J. O. Martinez, B. S. Brown, L. Isenhart and E. Tasciotti, *ACS Nano*, 2014, **8**, 9874–9883.
115 Z. Yang, W. Fan, W. Tang, Z. Shen, Y. Dai, J. Song, Z. Wang, Y. Liu, L. Lin, L. Shan, Y. Liu, O. Jacobson, P. Rong, W. Wang and X. Chen, *Angew. Chem., Int. Ed.*, 2018, **57**, 14101–14105.
116 F. Greco and M. J. Vicent, *Adv. Drug Delivery Rev.*, 2009, **61**, 1203–1213.
117 Y. Jiang, D. Cui, Y. Fang, X. Zhen, P. K. Upputuri, M. Pramanik, D. Ding and K. Pu, *Biomaterials*, 2017, **145**, 168–177.

118 H. Wang, W. Zhao, L. Zhou, J. Wang, L. Liu, S. Wang and Y. Wang, *ACS Appl. Mater. Interfaces*, 2018, **10**, 37–41.
119 W. Zhou, Y. Chen, Y. Zhang, X. Xin, R. Li, C. Xie and Q. Fan, *Small*, 2020, **16**, 1905641.
120 D. Cui, J. Huang, X. Zhen, J. Li, Y. Jiang and K. Pu, *Angew. Chem., Int. Ed.*, 2019, **58**, 5920–5924.
121 P. Sun, T. Huang, X. Wang, G. Wang, Z. Liu, G. Chen and Q. Fan, *Biomacromolecules*, 2020, **21**, 556–565.
122 C. Qian, J. Yu, Y. Chen, Q. Hu, X. Xiao, W. Sun, C. Wang, P. Feng, Q. Shen and Z. Gu, *Adv. Mater.*, 2016, **28**, 3313–3320.
123 Y. Wang, S. Li, P. Zhang, H. Bai, L. Feng, F. Lv, L. Liu and S. Wang, *Adv. Mater.*, 2018, **30**, 1705418.
124 T. Senthilkumar, L. Zhou, Q. Gu, L. Liu, F. Lv and S. Wang, *Angew. Chem., Int. Ed.*, 2018, **57**, 13114–13119.
125 A. Ribas and J. D. Wolchok, *Science*, 2018, **359**, 1350–1355.
126 C. Chen, X. Ni, S. Jia, Y. Liang, X. Wu, D. Kong and D. Ding, *Adv. Mater.*, 2019, **31**, 1904914.
127 J. Weiden, J. Tel and C. G. Figdor, *Nat. Rev. Immunol.*, 2018, **18**, 212–219.
128 J. Li, D. Cui, J. Huang, S. He, Z. Yang, Y. Zhang, Y. Luo and K. Pu, *Angew. Chem., Int. Ed.*, 2019, **58**, 12680–12687.
129 A. Lewis-Ballester, K. N. Pham, D. Batabyal, S. Karkashon, J. B. Bonanno, T. L. Poulos and S. R. Yeh, *Nat. Commun.*, 2017, **8**, 1693.
130 S. Valastyan and R. A. Weinberg, *Cell*, 2011, **147**, 275–292.
131 J. Li, J. Huang, Y. Lyu, J. Huang, Y. Jiang, C. Xie and K. Pu, *J. Am. Chem. Soc.*, 2019, **141**, 4073–4079.
132 J. Li, D. Cui, Y. Jiang, J. Huang, P. Cheng and K. Pu, *Adv. Mater.*, 2019, **31**, 1905091.
133 Z. Zhou, X. Liu, D. Zhu, Y. Wang, Z. Zhang, X. Zhou, N. Qiu, X. Chen and Y. Shen, *Adv. Drug Delivery Rev.*, 2017, **115**, 115–154.
134 M. A. Kay, *Nat. Rev. Genet.*, 2011, **12**, 316–328.
135 H. Ye, M. Daoud-El Baba, R. Peng and M. Fussenegger, *Science*, 2011, **332**, 1565–1568.
136 Y. Lyu, D. Cui, H. Sun, Y. Miao, H. Duan and K. Pu, *Angew. Chem., Int. Ed.*, 2017, **56**, 9155–9159.
137 P. D. Hsu, E. S. Lander and F. Zhang, *Cell*, 2014, **157**, 1262–1278.
138 Y. Lyu, S. He, J. Li, Y. Jiang, H. Sun, Y. Miao and K. Pu, *Angew. Chem., Int. Ed.*, 2019, **58**, 18197–18201.
139 L. Li, Z. Yang, S. Zhu, L. He, W. Fan, W. Tang, J. Zou, Z. Shen, M. Zhang, L. Tang, Y. Dai, G. Niu, S. Hu and X. Chen, *Adv. Mater.*, 2019, **31**, 1901187.